



# Upgrading of dichloromethane to olefins by hydrodechlorination: Improving process efficiency by the addition of Fe to carbon nanotubes-supported Pd catalyst

Sichen Liu<sup>a</sup>, Ana Iglesias-Juez<sup>b</sup>, Ana B. Hungría<sup>c</sup>, Maria Martin-Martinez<sup>d</sup>, Jorge Bedia<sup>a</sup>, Juan José Rodríguez<sup>a</sup>, Luisa María Gómez-Sainero<sup>a,\*</sup>

<sup>a</sup> Departamento de Ingeniería Química, Facultad de Ciencias, Universidad Autónoma de Madrid, C/Francisco Tomás y Valiente, 7. Campus de Cantoblanco, 28049, Madrid, Spain

<sup>b</sup> Instituto de Catálisis y Petroleoquímica, CSIC, C/Marie-Curie 2, 28049 Madrid, Spain

<sup>c</sup> Departamento de Ciencia de los Materiales, Ingeniería Metalúrgica y Química Inorgánica, Facultad de Ciencias, Universidad de Cádiz, Campus Río San Pedro, E-11510, Puerto Real (Cádiz), Spain

<sup>d</sup> Grupo CyPS, Dto. Ingeniería Química y de Materiales, Universidad Complutense de Madrid, Avda. Complutense s/n, 28040 Madrid, Spain

## ARTICLE INFO

### Keywords:

Hydrodechlorination  
Dichloromethane  
Olefins  
Pd  
Bimetallic catalysts  
CNT

## ABSTRACT

Upgrading of waste dichloromethane to produce olefins has been performed by hydrodechlorination (HDC) using bimetallic catalysts consisting of Pd-Fe/CNT, Pd-Sn/CNT and Pd-Ag/CNT. Pd/CNT was also studied. Pd-Fe/CNT showed the best performance in terms of activity ( $X \approx 81\%$ ) and stability, with the highest selectivity to olefins ( $>60\%$ , mainly  $C_2H_4$ ), at  $350^\circ\text{C}$ , which could be mainly attributed to the existence of stable Pd-Fe interaction. Characterization results and density functional theory calculations suggest that incorporating Fe atoms into the Pd lattice changes its electronic and geometrical properties. Fe atoms show stronger dissociative adsorption of  $CH_2Cl_2$  than Pd ones, leading to lower activation energies for the dechlorination of  $CH_2Cl_2$  on the studied Pd-Fe (111), which also favors the formation of C-C bond between two adjacent  $CH_2^*$ , promoting the formation of  $C_2H_4$ . Pd-Sn and Pd-Ag catalysts hinder olefins formation, due to the non-reactive Sn atoms and significant metal segregation in case of Pd-Ag.

## 1. Introduction

Chloromethanes (CMs), particularly dichloromethane (DCM) and chloroform (TCM), are widely used in different chemical industries, leading to the generation of residual effluents [1]. However, as volatile organic compounds (VOCs), they are toxic, carcinogenic, and promote global warming problems [2]. Catalytic hydrodechlorination (HDC) is a valuable technology that can treat them effectively in the gas phase using moderate operating conditions [3], producing diverse non-chlorinated compounds such as methane and other paraffins and olefins by coupling of the dechlorinated intermediates. The selectivity to the different products could be regulated by selecting the proper catalysts and operating conditions [4]. The production of olefins such as ethylene ( $C_2H_4$ ) and propylene ( $C_3H_6$ ) seems more attractive since these compounds are essential chemical feedstocks employed in plastic and pharmaceutical industries, among many others. Consequently, the

reduction of chloromethane emissions by their valorization to essential products is of high interest.

Monochloromethane (MCM) dechlorination has been widely studied in the production of olefins using zeolite materials (such as ZSMs and SAPOs) as catalysts (Eq. (1)) [5–7]. However, due to the absence of hydrogen in the process, the catalysts are easily deactivated through the oligomerization of hydrocarbons, resulting in the formation of coke blocking the zeolite pores [8]. The HDC of TCM employing carbon materials as catalyst support for producing light olefins (Eq. (2)) has been previously studied in our group [4,9–11]. Compared to other noble metals (Pt, Ru, Rh), using Pd as active phase resulted in a higher selectivity to C2-C3 hydrocarbons to the detriment of methane [9]. The Pd supported on mesoporous active carbon prepared from lignin through chemical activation [4], bimetallic Pd-Ag supported on commercial active carbon [10], and Pd supported on carbon nanotubes (CNT) [11] have demonstrated high catalytic activities in the HDC of

\* Corresponding author.

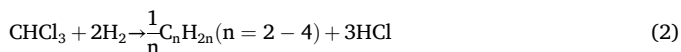
E-mail address: [luisa.gomez@uam.es](mailto:luisa.gomez@uam.es) (L.M. Gómez-Sainero).

<https://doi.org/10.1016/j.cej.2024.152128>

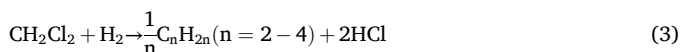
Received 25 January 2024; Received in revised form 6 May 2024; Accepted 9 May 2024

1385-8947/© 2024 The Authors. Published by Elsevier B.V. This is an open access article under the CC BY-NC license (<http://creativecommons.org/licenses/by-nc/4.0/>).

TCM with high selectivities to olefins, mainly owing to their small size of active centers and high electron density [4,9–11].



In a previous study [12], the HDC of DCM to produce olefins (Eq. (3)) was studied using Pd-based catalysts supported on zeolites, where the highest selectivity to olefins obtained was *ca.* 35 % when employing a L-type zeolite with only *ca.* 25 % conversion of DCM. These results highlight the necessity of designing more effective catalysts for the HDC of DCM to olefins. Different strategies can be taken to increase the selectivity towards olefins: promoting the adsorption of DCM instead of H<sub>2</sub>, and/or increasing the Pd dispersion or the electron density of Pd sites. In this sense, a second metal addition to Pd catalysts may be a feasible strategy to modulate all these key factors. Combinations with other metals have been previously explored, showing exciting properties for dehalogenation reactions in this sense. For instance, we demonstrated that by adding Ag to a Pd catalyst, due to their different electronegativity, the Ag atoms could reduce the Pd ones, leading to a higher proportion of Pd<sup>0</sup> and favoring the formation of olefins [4] as it is known that Pd<sup>n+</sup> shows stronger interaction with the formed olefins, thus favoring their further hydrogenation to paraffins [4]. Other example are Pd-Fe catalysts that showed high catalytic stability in the HDC of tetrachloromethane due to the high dispersion and suitable metallic proportion, resulting in high selectivities to C<sub>2</sub>-C<sub>4</sub> hydrocarbons [13]. Bimetallic Pd-Sn catalysts also exhibited high efficiency in the Heck dehalogenation of iodobenzene, probably due to the reduction of Pd<sup>2+</sup> by Sn<sup>2+</sup> during the catalyst preparation [14].



Not only is the metallic component important, but the support also plays an important role. Active carbon-supported Pd catalysts usually deactivate strongly during the HDC of DCM by forming Pd carbide (PdC<sub>x</sub>) [15]. On the contrary, structured carbon materials, such as multiwalled carbon nanotubes (CNT), might be more suitable as support in this reaction. CNT present excellent mechanical and thermal stability, coke-free catalytic performance, and could promote strong metal-support interactions [16–18]. Furthermore, CNT would have fewer diffusional problems than porous carbon materials [19] and have an electron-donor character [11].

Based on all this, the main purpose of this study is to formulate suitable bimetallic Pd catalysts supported on CNT for the HDC of DCM to olefins. The objectives include preparing Pd with Fe, Sn, or Ag, CNT-supported catalysts, evaluating their activity and selectivity at different reaction conditions, and determining their physicochemical properties by using several characterization techniques to learn the key properties that maximize the production of light olefins. Monometallic Pd supported on CNT (Pd/CNT) is also studied for comparison purposes. Moreover, density functional theory (DFT) calculations were performed to fully understand the reaction mechanism at the atomic level, focusing on the formation of light olefins.

## 2. Materials and methods

### 2.1. Catalyst preparation

Commercial multiwalled CNT (Sigma-Aldrich) with diameters of 110–170 nm and lengths of 5–9 μm were employed as support for the synthesis of Pd-M/CNT (M = Fe, Sn, or Ag) catalysts via incipient wetness impregnation. The CNTs were first impregnated with an aqueous solution of FeCl<sub>3</sub> (>99 %, Sigma-Aldrich), SnCl<sub>2</sub> (>99 %, Sigma-Aldrich), or AgNO<sub>3</sub> (>99 %, Sigma-Aldrich) to obtain a nominal

load of 0.5 wt% of the respective metal. Then, the three samples were dried at 100 °C for 2 h with a heating rate of 20 °C h<sup>-1</sup>. After that, the impregnation process was repeated, employing an acidic aqueous solution of PdCl<sub>2</sub> (>99 %, Sigma-Aldrich) with an adequate concentration to get a nominal 1.0 wt% of Pd. The same process was used to prepare the Pd/CNT catalyst. Finally, the five dried samples were activated via reduction employing a continuous H<sub>2</sub> (99.999 %, Nippon Gases) flow of 50 Ncm<sup>3</sup> min<sup>-1</sup> at 350 °C for 2 h before the reaction.

### 2.2. Catalyst characterization

N<sub>2</sub> adsorption-desorption at –196 °C was employed to analyze the porous structure of the catalysts using a Micromeritics equipment (Tristar II 3020). The samples were degassed at 150 °C for 12 h before the measurement. The surface areas (S<sub>BET</sub>) were calculated using the Brunauer – Emmett – Teller (BET) method. The set P/Po range for BET linear analysis was 0.05 to 0.20, using ten points for the fitting and a N<sub>2</sub> cross-section of 16.2 Å<sup>2</sup>.

The catalysts' surface composition was measured by X-ray photoelectron spectroscopy (XPS) on a Physical Electronics 5700C X-ray photoelectron spectrometer using MgKα radiation of 1253.6 eV. The elemental surface compositions of each sample were obtained by general spectra recorded by scanning binding energy (BE) in a range of 0–1200 eV. The BE changes aroused by sample charging could be corrected by C1s peak (284.5 eV) working as an internal standard. The deconvolution of XPS spectra was performed using mixed Gaussian-Lorentzian component profiles with a least-squares method after Shirley background subtraction. The relative atomic proportion of each species was calculated through the area of the related peak deconvoluted from core-level curves according to Wagner sensitivity factors [20].

X-ray diffraction (XRD) was used to analyze the crystalline structure of the catalysts. The XRD patterns were obtained in an X'Pert PRO PANalytical diffractometer associated with an X'Celerator RTMS detector. A CuKα (α = 0.15406 nm) monochromatic radiation and a Ge mono filter were used to scan powdered catalysis samples. A scanning range (2θ) of 10–90° with a scan step size of 0.0334 were used. Signal information was collected every 200 s.

Scanning Transmission Electron Microscopy (STEM) imaging was performed using a double-corrected FEI Titan<sup>3</sup> 60–300 Themis microscope operated at 200 kV in High Angle Annular Dark Field Scanning Transmission Electron Microscopy (HAADF-STEM) mode. Samples were characterized by spectrum imaging technique (SI) through X-ray energy dispersive spectroscopy (XEDS) to obtain the local distribution of all elements present. The HAADF-STEM images were recorded using a convergence semi-angle α ≈ 19 mrad, a spot size of 9, and a beam current of 30 pA. In the case of microanalysis experiments, the beam current was increased to 100–120 pA, using a dwell time ranging from 50–75 μs per pixel, an image size of 512 x 512 pixels. Each spectrum-image data set was collected as a series of frames using a drift compensation tool. All HAADF-STEM and SI-XEDS data sets were acquired and processed using Velox software.

The metal loading composition in the catalysts samples was quantified by total-reflection X-ray fluorescence (TXRF), employing a TXRF 8030C spectrometer (Cameca, France) equipped with a 3 kW X-ray tube with a Mo/W alloy anode connected to a double-W/C multilayer monochromator. A Si(Li) detector with an 80 mm<sup>2</sup> active area, whose resolution was 150 eV at 5.9 keV (Oxford Instruments, England), was used. The samples were measured at 50 kV with an auto-adjusted intensity to achieve a count rate of approximately 8500 cps. The signals were collected every 500 s.

X-ray spectroscopy (XAS) analysis was performed to study the electronic properties of Pd atoms and their local environment. The measurements were carried out at ALBA Synchrotron CLAES beamline. The *in-situ* temperature-programmed reduction (TPR) of the fresh catalysts were performed using a solid-gas multipurpose cell where auto-supported samples were placed. A double-crystal Si(111)

monochromator was used to collect Pd K-edge XAS spectra in fluorescence mode. A mass spectrometer was employed to monitor the reaction progress and perform leak checks by connecting to the outlet. The *in-situ* TPR was realized under a mixture of H<sub>2</sub>/N<sub>2</sub> (5/95 M ratio) increasing temperature from room temperature (RT) to 350 °C, collecting *in-situ* X-ray absorption near edge structure (XANES) spectra during the ramp. Finally, after cooling to RT, extended X-ray absorption fine structure (EXAFS) spectra were registered. Spectra were normalized using the Athena program included in the Demeter package 0.9.26 [21].

### 2.3. Catalyst testing

The catalytic behavior of the fresh-reduced catalysts (Pd-Fe/CNT, Pd-Sn/CNT, Pd-Ag/CNT, and Pd/CNT) was tested in the HDC of DCM. A continuous flow reaction system, PID Microactivity (Micromeritics, USA) was employed [22], using a quartz bed micro-reactor with a 9 mm internal diameter. A gas-chromatograph (Agilent 7820A) with a capillary column (CP-SilicaPLOT, 60 m × 0.53 mm internal diameter, Agilent, Madrid, Spain) was connected to the reaction system to analyze the concentration of reactants and products using a Flame Ionization Detector (FID). The experiments were operated at atmospheric pressure and 350 °C. The temperature was controlled and monitored using a thermocouple inserted in the catalyst bed. Nitrogen was used as balance gas until 100 Ncm<sup>3</sup>/min total flow rate, being the DCM inlet concentration 1000 ppm<sub>v</sub>. Different H<sub>2</sub>/DCM molar ratios (50:1 and 25:1) were tested. All the catalytic tests used a space-time (τ) of 0.2 kg h·mol<sup>-1</sup>, finding no external mass or heat transfer limitations.

The behavior of the catalysts in the HDC reactions was analyzed in terms of DCM conversion (X(DCM)), selectivity (S(i)), and yield (Y(i)) to the main products, determined by the Eqs. (4), (5) and (6). The error of mass balance, calculated by the Eq. (7), was lower than 5 %.

$$X(\text{DCM}) = \frac{C(\text{DCM})_{\text{in}} - C(\text{DCM})_{\text{out}}}{C(\text{DCM})_{\text{in}}} \times 100 \% \quad (4)$$

$$S(i) = \frac{C(i)_{\text{out}} \times N(\text{Carbon})_i}{C(i)_{\text{out}} \times N(\text{Carbon})_i + C(j)_{\text{out}} \times N(\text{Carbon})_j + \dots} \times 100 \% \quad (5)$$

$$Y(i) = \frac{C(i)_{\text{out}} \times N(\text{Carbon})_i}{C(\text{DCM})_{\text{in}}} \times 100 \% \quad (6)$$

$$\text{error of mass balance} (\%) = \frac{C(\text{DCM})_{\text{in}} - [C(i)_{\text{out}} \times N(\text{Carbon})_i + C(j)_{\text{out}} \times N(\text{Carbon})_j + \dots]}{C(\text{DCM})_{\text{in}}} \times 100 \% \quad (7)$$

where C(DCM)<sub>in</sub> and C(DCM)<sub>out</sub> correspond to the concentration of DCM in the total flow at the inlet and outlet of the microreactor, respectively, C(i)<sub>out</sub>, C(j)<sub>out</sub>, etc. are related to concentrations of the products i, j, etc., respectively, in the outlet flow of the microreactor, and N(Carbon)<sub>i</sub>, N(Carbon)<sub>j</sub>, etc. correspond to the number of carbon atoms in the products i, j, etc., respectively.

### 2.4. Computational methods

The Vienna ab initio simulation package (VASP 5.4.4) [23,24] was employed for the DFT calculations. Different slab models represented as pure metal or bimetallic systems were studied. Generalized gradient approximation with the Perdew – Burke – Ernzerhof (GGA-PBE) functional was used to obtain the exchange – correlation energies [25]. The spin polarization was set when needed. Projector-augmented wave

(PAW) was used to describe the inner electrons, while the valence monoelectronic states were represented using plane waves with an energy cutoff of 450 eV. The Brillouin zone was described by a Γ-centered k-point grid of 3 × 3 × 1. Van der Waals interactions were described through the DFT-D3 method [26].

The Pd-Fe bimetallic and Pd monometallic systems were simulated. The Pd monometallic system worked as a blank essay to be compared with the bimetallic system. The Pd-Fe system was set with a 1 (Pd): 1 (Fe) atomic proportion. According to a previous study [27], at the reduction and reaction temperature used (350 °C), the Pd<sub>2</sub>-Fe<sub>2</sub> face-centered cubic (fcc) crystal structure is the most stable one. Thus, fcc was used to model the Pd-Fe bimetallic structure compared to the pure Pd structure, shown in Fig. 1. The optimized lattice constants were a = b = 3.8370 Å & c = 3.7592 Å for Pd-Fe and 3.9405 Å for Pd. The gas-phase molecules of reactants and main products were optimized in a space of 15 Å. The Pd-Fe and Pd were modeled in the (1 1 1) surface with a four-layer p(4 × 4) slab. The two bottom layers were fixed in the bulk lattice in all slabs, while the two top layers and the adsorbents were allowed to relax. The slabs were interspaced through a vacuum space of 15 Å along the z-direction, correcting the arising dipole. The convergence thresholds were 0.03 eV Å<sup>-1</sup> for ionic relaxing steps and 10<sup>-5</sup> eV for electronic relaxing steps.

The adsorption energy (E<sub>ads</sub>) of the reactants was calculated in the following way (Eq. (8)):

$$E_{\text{ads}} = E_{\text{reactant-surface}} - E_{\text{surface}} - E_{\text{reactant, gas-phase}} \quad (8)$$

Where E<sub>reactant-surface</sub> is the total energy of the reactant adsorption on the surface, E<sub>surface</sub> is the total energy of the clean surface, and E<sub>reactant, gas-phase</sub> is the total energy of the reactant in vacuum space.

A climbing image nudged elastic band (CI-NEB) method [28,29] was applied to identify the transition states (TSs) and the activation energy in the reaction profiles. The TSs were verified by vibrational frequency analyses [29], where a single imaginary frequency would be found along the reaction coordinate. Moreover, Gibbs free energy corrections for the reaction temperature (350 °C) were performed using VASPKIT, contributing the zero-point energy, entropy, and enthalpy. For adsorbed species, the Gibbs free energies considered the vibrational contribution of all degrees of freedom [30].

## 3. Results and discussion

### 3.1. HDC tests

Fig. 2(a and b) show the evolution of DCM conversion with the different catalysts in the HDC reaction at 350 °C with an H<sub>2</sub>/DCM molar ratio of 50 and the initial values of the selectivities to the main reaction

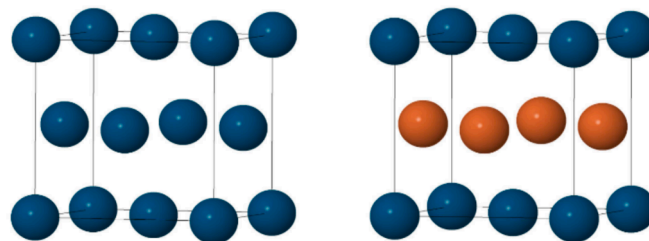
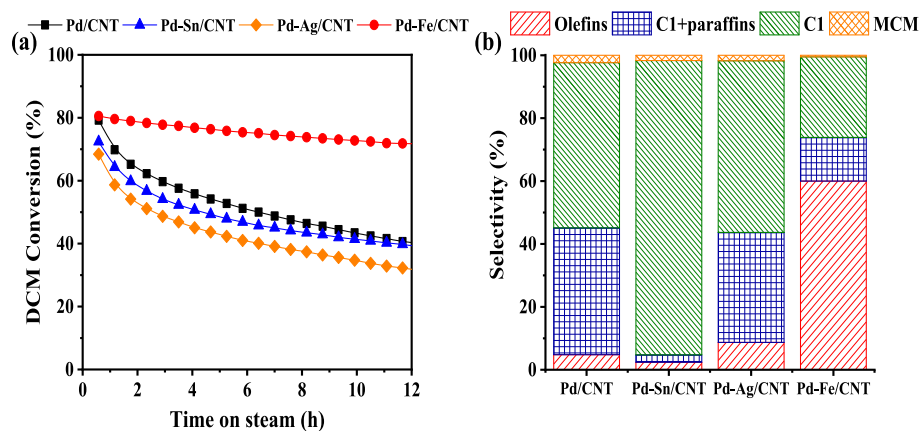


Fig. 1. Pd bulk (left) and Pd-Fe bulk (right) (blue ball: Pd atom; orange ball: Fe atom).



**Fig. 2.** Performance of the catalysts in the HDC of DCM, (a) DCM Conversion, (b) Initial selectivity to products. ( $\tau = 0.2 \text{ kg h}^{-1} \text{ mol}^{-1}$ ;  $T_{\text{reaction}} = T_{\text{reduction}} = 350 \text{ }^{\circ}\text{C}$ ;  $\text{H}_2/\text{DCM} = 50$ ).

products, respectively. The products generated in the reaction are olefins ( $\text{C}_2\text{H}_4$  and traces of  $\text{C}_3\text{H}_6$  and 1- $\text{C}_4\text{H}_8$ ), C1 ( $\text{CH}_4$ ), C1 + paraffins ( $\text{C}_2\text{H}_6$  and traces of  $\text{C}_3\text{H}_8$  and n- $\text{C}_4\text{H}_{10}$ ) and traces of monochloromethane (MCM). The evolution of the selectivities to the products with reaction time is shown in Fig. S1. In general, the selectivities to  $\text{CH}_4$ ,  $\text{C}_2\text{H}_4$ , and  $\text{C}_2\text{H}_6$  are considerably higher than to the other products, contrary to what was previously observed during the HDC of TCM, which resulted in more diverse byproducts [4].

As shown in Fig. 2(a), Pd-Fe/CNT offers the highest and most stable DCM conversion, with an initial value of ca. 81 %. After 12 h of reaction, only 9 % of DCM conversion was lost (final conversion: ca. 72 %). Pd/CNT showed a similar initial DCM conversion (ca. 79 %) compared to Pd-Fe/CNT, but it decreased quickly during the reaction. The other two bimetallic catalysts show some lower initial DCM conversions (Pd-Sn/CNT: ca. 72 %; Pd-Ag/CNT: ca. 68 %) than the Pd/CNT, which also suffered stronger deactivation during the reaction (see Fig. 2(a)).

Regarding the selectivity, when using the monometallic Pd/CNT, the main reaction product is  $\text{CH}_4$ , with an initial selectivity of 53 % that remained practically constant during the reaction, followed by  $\text{C}_2\text{H}_6$ , with around 30 % of selectivity (see Fig. S1(a)). The initial selectivity to the target olefins only presented 5 % (mainly  $\text{C}_2\text{H}_4$ ), and although it enhanced to 10 % after 12 h of reaction, this value is still undoubtedly low. On the contrary, the addition of Fe dramatically improved the production of olefins: Pd-Fe/CNT gave an outstanding selectivity to olefins (>60 %, mainly  $\text{C}_2\text{H}_4$ ), much higher than the rest of the catalysts, which remained practically stable during the reaction (see Fig. S1(b)).

Besides  $\text{C}_2\text{H}_4$ , the other main reaction products obtained with Pd-Fe/CNT were  $\text{CH}_4$  (ca. 25 %) and  $\text{C}_2\text{H}_6$  (ca. 13 %). Regarding the other

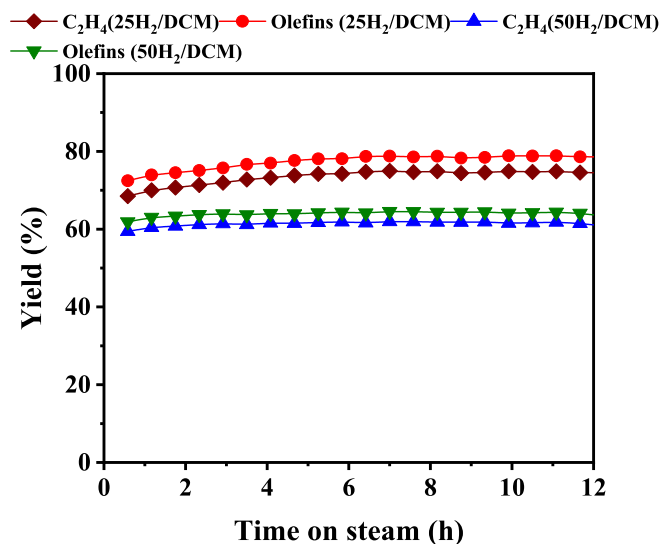


**Fig. 4.** Evolution of yields to  $\text{C}_2\text{H}_4$  and total olefins in the HDC of DCM ( $\tau = 0.2 \text{ kg h}^{-1} \text{ mol}^{-1}$ ;  $T_{\text{reaction}} = T_{\text{reduction}} = 350 \text{ }^{\circ}\text{C}$ ;  $\text{H}_2/\text{DCM} = 50$  and 25).

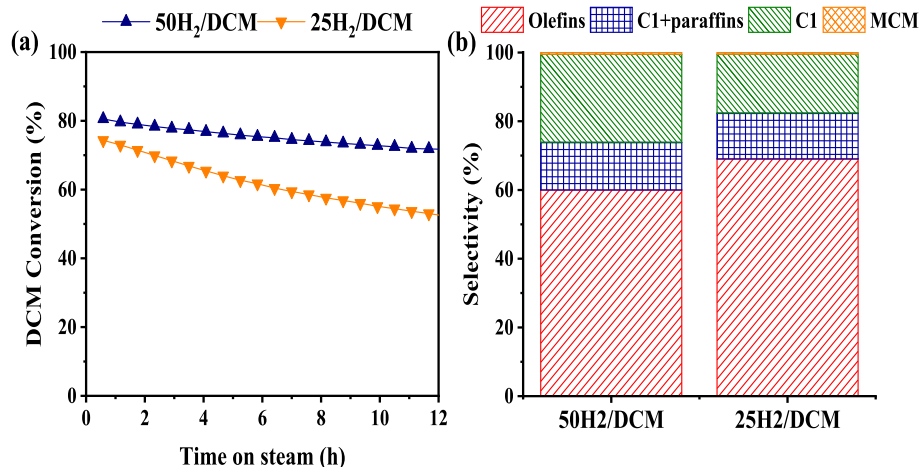


**Fig. 3.** Performance of Pd-Fe/CNT in the HDC of DCM, (a) Conversion of DCM, (b) Initial selectivity to products. ( $\tau = 0.2 \text{ kg h}^{-1} \text{ mol}^{-1}$ ;  $T_{\text{reaction}} = T_{\text{reduction}} = 350 \text{ }^{\circ}\text{C}$ ;  $\text{H}_2/\text{DCM} = 50$  and 25).



bimetallic catalysts, Pd-Sn/CNT presented an extremely high selectivity to CH<sub>4</sub> (94 %, see Fig. 2(b) and S1(c)), Pd-Ag/CNT showed the following distributions of selectivities: CH<sub>4</sub> (ca. 55 %) > C1 + paraffins (ca. 35 %, mainly C<sub>2</sub>H<sub>6</sub>) > olefins (ca. 8 %, mainly C<sub>2</sub>H<sub>4</sub>) > MCM (ca. 2 %) similar as Pd/CNT (see Fig. 2(b) and S1(a and d)).

For the most active and stable catalyst, the Pd-Fe/CNT catalyst, the effect of the H<sub>2</sub>/DCM ratio was analyzed. Fig. 3(a and b) compare the DCM conversions and initial selectivities, respectively, at H<sub>2</sub>/DCM ratios of 25 and 50 using the Pd-Fe/CNT catalyst. The time evolution of the selectivities with H<sub>2</sub>/DCM = 25 is shown in Fig. S2. Besides, the time evolution of the yields to total olefins and specifically C<sub>2</sub>H<sub>4</sub> during the reactions is depicted in Fig. 4. Meanwhile, the time evolution of the yields to all products is shown in Fig. S3. As seen in Fig. 3, with the lower H<sub>2</sub>/DCM ratio of 25, the initial selectivity to olefins enhanced up to 70 %, with a slight increase during the reaction (see Fig. S2). Furthermore, C<sub>2</sub>H<sub>4</sub> was still the main olefin produced with more than 65 % selectivity. Although the lower H<sub>2</sub>/DCM ratio resulted in a lower DCM conversion, the yield to olefins (ca. 75 %) was still significantly higher than that obtained with an H<sub>2</sub>/DCM molar ratio of 50 (ca. 62 %) (see Fig. 4). Regardless of the H<sub>2</sub>/DCM ratio, C<sub>2</sub>H<sub>4</sub> was the main olefin produced.

The results show that H<sub>2</sub> concentration kinetically affects the activity of Pd-Fe/CNT and selectivity to C<sub>2</sub>H<sub>4</sub>, which will be further studied in DFT calculations in Section 3.3.

### 3.2. Characterization

The BET surface areas of the four catalysts are summarized in Table S1. All fresh-reduced catalysts present similar S<sub>BET</sub> around 100 m<sup>2</sup>/g. No significant changes are observed for the used catalysts, suggesting that carbonaceous deposits are not formed on the catalysts during the HDC reaction.

The deconvoluted Pd 3d, Fe 2p, Sn 3d, Ag 3d and Cl 2p regions in XPS profiles of fresh-reduced and/or used catalysts are presented in Figs. 5, S4 and S5. The signals of Pd 3d, Fe 2p, Sn 3d and Ag 3d can be

deconvoluted into doublets which can be separated by 5.26 eV (Pd 3d<sub>5/2</sub> and Pd 3d<sub>3/2</sub>), 13.6 eV (Fe 2p<sub>3/2</sub> and Fe 2p<sub>1/2</sub>), 8.41 eV (Sn 3d<sub>5/2</sub> and Sn 3d<sub>3/2</sub>) and 6.0 eV (Ag 3d<sub>5/2</sub> and Ag 3d<sub>3/2</sub>) [31]. The signals of Cl 2p can be deconvoluted into 3 peaks at binding energies around 198.0 eV, 200.4 eV and 202.1 eV. The Cl 2p peak at 198.0 eV is related to inorganic chlorides and the other two peaks are related to organic chlorides [32]. The atomic concentrations of metals and chlorine, and proportions of metallic and chloride species on all the catalysts' surfaces are summarized in Tables S2 and S3, respectively.

When analyzing the Pd 3d<sub>5/2</sub> XPS region of monometallic Pd/CNT, the peak at around 335.6 eV (see Fig. 5) is related to zero-valent Pd (Pd<sup>0</sup>). In comparison, the one at 338.1 eV is associated with electro-deficient Pd (Pd<sup>n+</sup>) [33]. As shown in Fig. 5 and Table S3, the proportion of Pd<sup>0</sup> is greater than that of Pd<sup>n+</sup>, which is also observed in the bimetallic catalysts. The formation of Pd<sup>n+</sup> could be mainly related to the metal-support interaction. Somewhat Cl concentration is observed in the used Pd/CNT (0.03 %, see Table S2) that, according to XPS results, has inorganic and organic proportions (organic chlorides: 74.8 %; inorganic chlorides: 25.2 % see Table S3 and Fig. S5). As the organic proportion is more evident, it is suggested that some formed chlorinated intermediate hydrocarbons are adsorbed on the Pd centers during the reaction, which may affect the activity of the catalyst.

In Pd-Fe/CNT, a shift to higher binding energy is observed on the Pd<sup>0</sup> peak (335.9 eV, see Fig. 5) compared to its value on Pd/CNT (335.6 eV). In addition, the Fe 2p<sub>3/2</sub> region shows a peak at 711.2 eV related to the presence of Fe<sup>3+</sup>, which is also shifted respecting the typical value (711.6 eV) (see Fig. S4(a)) [34]. The peak present at 717.4 eV could be related to the Fe satellite [35] (Fig. S4(a)).

Previous studies [36,37] suggested that the binding energy shifts might be aroused by the initial state effects (e.g., electron transfer), orbital rehybridization, and final state effects arising from the formation of Pd-Fe interaction. When comparing fresh and used catalysts, no significant changes are observed in the binding energy of Pd and Fe related peaks (see Figs. 5(a) and S4 with similar atomic compositions (see

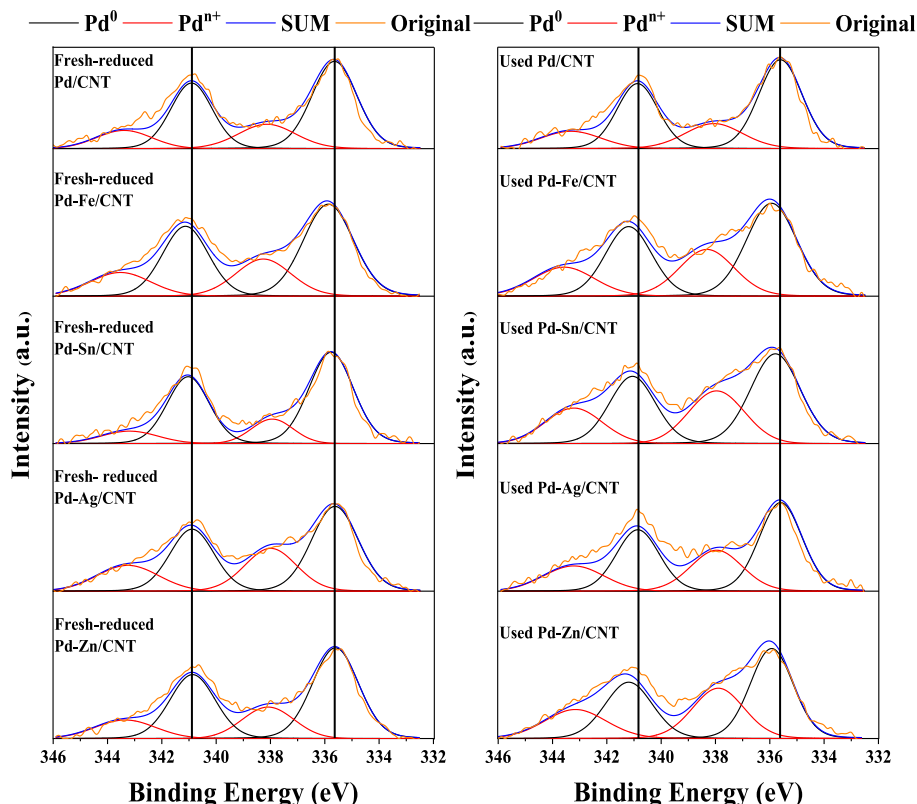


Fig. 5. XPS results of Pd spectra in fresh-reduced and used catalysts.

Table S2). This suggests that a stable Pd-Fe interaction is formed in Pd-Fe centers, which could contribute to the stability of Pd-Fe/CNT (see Fig. 2(a)).

The Fe remains completely oxidized in the fresh-reduced and used catalysts (see Fig. S4(a)). The used Pd-Fe/CNT shows some Cl atomic concentration (0.10 %, see Table S2) with similar organic chlorides and inorganic chlorides proportions (inorganic chlorides: 48.2 %; organic chlorides: 51.7 %, see Fig. S5 and Table S3), suggesting the adsorption of some produced chlorides on the catalyst surface, which may downgrade the stability of the catalyst when reducing H<sub>2</sub> covering (reduction of H<sub>2</sub>/DCM molar ratio from 50 to 25, see Fig. 3(a)).

A slight shift of the Pd<sup>0</sup> peak to higher binding energy is observed on Pd-Sn/CNT (335.8 eV, see Fig. 5) regarding Pd/CNT, suggesting some effect of Sn atoms on the Pd ones. It could indicate a Pd-Sn interaction in the active centers [37,38], but this interaction is not clearly evidenced due to the slight binding energy displacement. The Sn 3d<sub>5/2</sub> peak at 486.6 eV (fresh catalyst) or 486.5 eV (used catalyst) (Fig. S4(b)) can be related to Sn<sup>2+</sup> [39]. A decrease in Sn atomic composition and Pd<sup>0</sup> proportion is observed on the surface of the catalyst used (Table S2 and S3, respectively), which may contribute to the lower stability of this catalyst (see Fig. 2(a)). The used catalyst shows some Cl atomic concentration (0.05 %, see Table S2) on the catalyst surface, with a higher proportion of organic chlorides (organic chlorides: 61.0 %; inorganic chlorides: 39.0 %, see Table S3 and Fig. S5), suggesting the adsorption of chlorides on active centers. In addition, incorporating Sn to Pd catalyst downgrades the formation of olefins, with a significant increase of methane selectivity, which could be ascribed to the inability of Sn atoms to adsorb any carbon atoms according to previous DFT studies [37,40,41].

On Pd-Ag/CNT, no significant shift is observed on Pd<sup>0</sup> peak (335.6 eV, see Fig. 5) compared to Pd/CNT, although the Ag3d<sub>5/2</sub> region

presents peaks at 368.5 eV (Ag<sup>0</sup>) and 367.9 eV or 367.8 eV (Ag<sup>+</sup>) (see Fig. S4(c)), similar as the values shown in previous studies where Pd-Ag alloys are formed [41,42]. Therefore, Pd-Ag interactions cannot be confirmed by the XPS analysis. Despite being lower than in the other catalysts, again, most of Pd appears as Pd<sup>0</sup>, both in the fresh and used catalyst (64 %, see Table S3), but a decrease in Pd surface composition is observed after the reaction (fresh-reduced catalyst: 0.26 %, used catalyst: 0.16 %, see Table S2) which could contribute to the low stability of the catalyst. In addition, a significant decrease of zero-valent Ag<sup>0</sup> is observed after the reaction (from 70.7 % to 38.6%). Ag active centers may be oxidized by the adsorbed chlorinated hydrocarbons [10], such as DCM and chlorinated intermediates. Some Cl atomic concentration (0.08 %, see Table S3) is observed in the used catalyst (inorganic chlorides: 49.1 %; organic chlorides: 50.9 %, see Fig. S5 and Table S3). All this may explain this catalyst's low activity and instability (see Fig. 2(a)).

The XRD patterns of the fresh-reduced and used catalysts are shown in Fig. 6. The characteristic peaks related to the structure of CNT (C(002), C(100), C(101), C(102), C(004), C(110), C(112)) are observed and identified in agreement to previous studies [43,44]. No significant signals related to metallic structure facets are observed in the fresh and used Pd/CNT, Pd-Fe/CNT, and Pd-Sn/CNT, probably due to their small nanoparticle (NP) sizes. The XRD patterns of the fresh-reduced and used Pd-Ag/CNT show two peaks at 38.12° and 64.42° corresponding to Ag(111) and Ag(220), respectively [45]. The presence of these peaks could be due to the large sizes of isolated Ag NPs, which become even bigger in the used catalyst, suggesting the sintering of Ag NPs during the reaction. Since the big Ag NPs have shown low activity in a previous HDC of TCM study [10], the sintering of Ag NPs could also contribute to downgrade the stability of the catalyst.

The HAADF-STEM images of all fresh-reduced catalysts and the

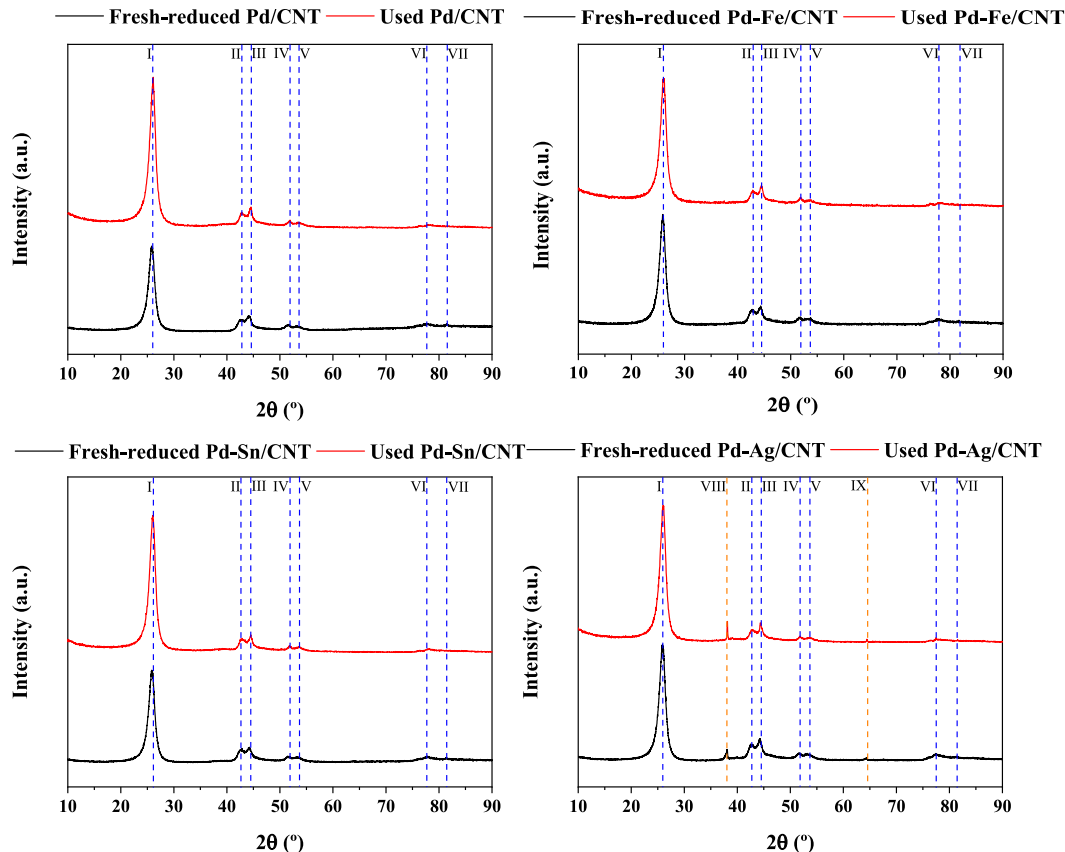
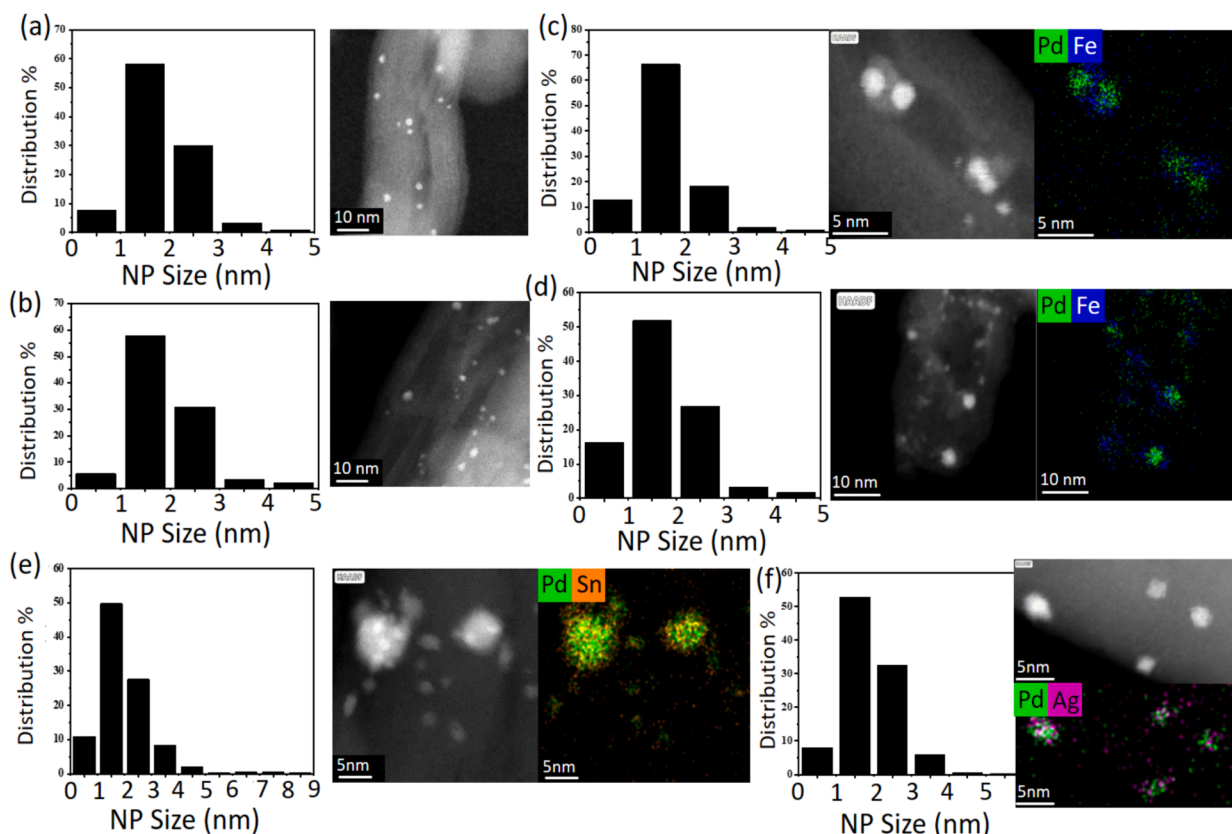


Fig. 6. XRD results of fresh-reduced and used catalysts (I: C(002); II: C(100); III: C(101); IV: C(102); V: C(004); VI: C(110); VII: C(112); Pd-Ag/CNT: VIII: Ag(111); IX: Ag(220)).



**Fig. 7.** HAADF-STEM images of the fresh-reduced and used catalysts ((a) fresh-reduced and (b) used Pd/CNT; (c) fresh-reduced and (d) used Pd-Fe/CNT; (e) fresh-reduced Pd-Sn/CNT; (f) fresh-reduced Pd-Ag/CNT) with the distribution of NP sizes in each catalyst.

**Table 1**  
Mean NP size of catalysts.

	Fresh-reduced Pd/CNT	Used Pd/CNT	Fresh-reduced Pd-Fe/CNT	Used Pd-Fe/CNT	Fresh-reduced Pd-Sn/CNT	Fresh-reduced Pd-Ag/CNT
Mean NP Size(nm)	1.8	1.9	1.6	1.7	2.0	1.9

elemental mapping analysis of bimetallic NPs, together with the distribution of NPs sizes, are shown in Fig. 7. More than 200 nanoparticles of each catalyst are used to calculate the distribution of NPs sizes. The mean metal NPs sizes of fresh-reduced and used catalysts are summarized in Table 1. The atomic fractions obtained from EDS spectra of bimetallic catalysts are presented in Table 2. Regarding the distributions (see Fig. 7), most NPs present sizes between 1 and 2 nm, corresponding with their mean NP sizes in all fresh-reduced catalysts (see Table 1). Furthermore, similar small NPs are observed in the fresh-reduced and used catalysts (Pd/CNT and Pd-Fe/CNT) (see Fig. 7(b and d)) in agreement with the XRD results (see Fig. 6). Herein, the different activities shown by the catalysts cannot be attributed to differences in their NPs sizes, but to the other mono- and bimetallic effects, except for Pd-Ag/CNT where big Ag NPs and sintering of Ag NPs are observed in the

**Table 2**  
Metallic composition of catalysts.

	TXRF composition (at.%)				HAADF-STEM Atomic Fraction (at. %)			
	Pd	Fe	Sn	Ag	Pd	Fe	Sn	Ag
Pd/CNT	1.00	—	—	—	—	—	—	—
Pd-Fe/CNT	0.90	1.00	—	—	55	45	—	—
Pd-Sn/CNT	0.93	—	0.51	—	65	—	34	—
Pd-Ag/CNT	0.87	—	—	0.20	—	—	—	—

fresh-reduced and used catalysts respectively shown by XRD results (see Fig. 6).

The elemental mapping analysis images (see Fig. 7(c and d)) show that the Pd-Fe/CNT presents bimetallic Pd-Fe nanoparticles (mainly heterogeneous) on the fresh-reduced and used catalysts. Moreover, the atomic fraction of Pd-Fe nanoparticle is Pd: Fe = 55: 45  $\approx$  1: 1, very close to the target theoretical value in sample preparation and similar to the TXRF composition (0.90: 1.00, see Table 2).

The Pd-Sn/CNT clearly presents Pd-Sn homogeneous NPs, with some of them slightly enriched in Sn at the surface level (see Fig. 7(e)). Meanwhile, its atomic fraction (Pd: Sn = 66: 34  $\approx$  2: 1, see Table 2) closely aligns with its TXRF composition (Pd: Sn = 0.93: 0.51, see Table 2). The homogeneous distribution of Sn appears to dilute Pd centers, however its distribution would not be stable since there is an evident decrease of Sn atomic composition in the used catalyst (see Table S2). At the same time, some previous DFT studies [38,46,47] confirm that Sn species cannot adsorb carbon atoms, this homogeneous distribution of Sn on Pd-Sn centers could downgrade the activity and prevent the oligomerization of carbonaceous species owing to the extension of Pd-Pd distance by the incorporation of Sn atoms favoring the formation of CH<sub>4</sub> to the detriment of olefins. Therefore, during the reaction, CH<sub>4</sub> became the only main product on Pd-Sn/CNT when operating with an excess of H<sub>2</sub> (H<sub>2</sub>/DCM = 50) (see Fig. 2(b) and S1(c)).

In the presented elemental mapping analysis image (see Fig. 7(e)), NPs with association of Ag and Pd atoms are observed. However, in

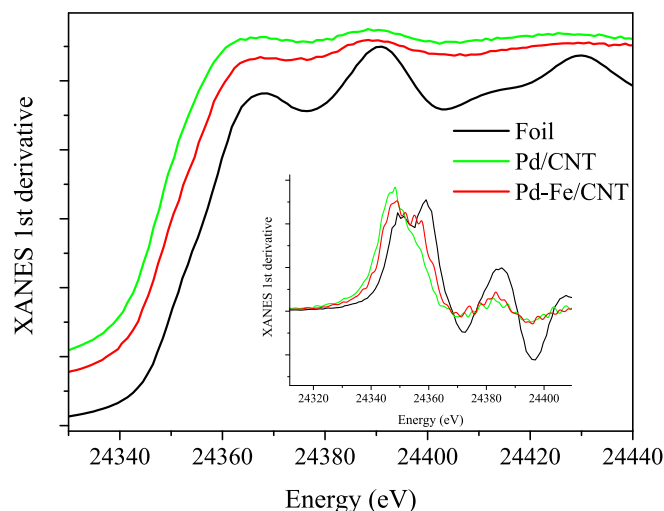


**Fig. 8.** Pd K-edge XANES spectra of the fresh-reduced samples Pd/CNT and Pd-Fe/CNT. XANES spectrum of the Pd foil has been included as a reference. The figure inset shows the first derivative of the XANES spectra.

many other images (not presented), the NPs do not contain any Ag atoms, in agreement with the XPS (see Fig. 5) and XRD (see Fig. 6) results, indicating that the interaction of Pd and Ag is not evident on the catalyst. As a result, the activity of Pd-Ag/CNT is similar but lower than that of Pd/CNT (see Fig. 2(a)), probably due to the existence of big Ag NPs and their sintering during the reaction confirmed by XRD results (see Fig. 6) where the Ag NPs could be oxidized by the adsorbed chlorides formed in the reaction (see Fig. S4(c) and Table S3). A Ni impurity was also observed in CNT support, but no influence in the activity results was detected, as determined by the performance of blank experiments.

To learn more about the causes of the great performance of the Pd-Fe/CNT catalyst, this catalyst and Pd/CNT are studied by XAS. Fig. 8 shows the XANES spectra of the Pd-species acquired after H<sub>2</sub> reduction. XANES features (edge position and continuum resonance (CR) characteristics) are unequivocally owing to Pd metallic species in an fcc-matrix [48]. Nevertheless, some differences are notified compared to the typical XANES spectrum of pure Pd (Pd-foil reference) in relation to the energy position of the edge and the CRs, as well as their intensity. Regarding the global intensity of the CRs, the differences are lower for

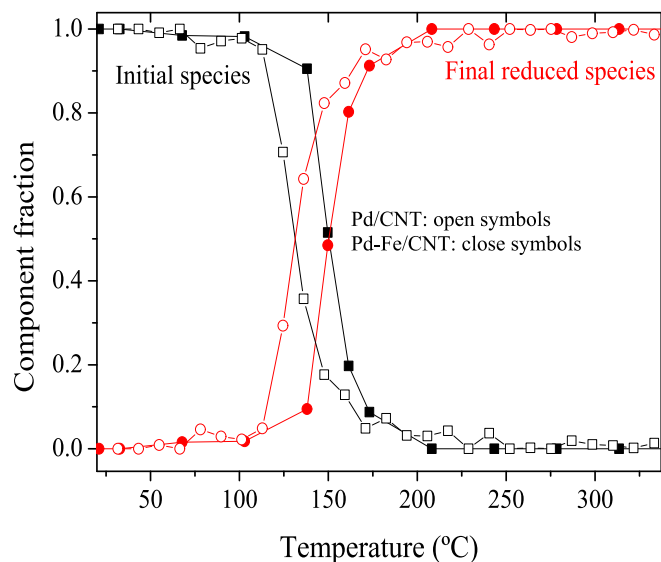


**Fig. 9.** Fraction evolution of initial (black) and final species (red) during TPR in H<sub>2</sub> for Pd/CNT and Pd-Fe/CNT: open and close symbols, respectively.

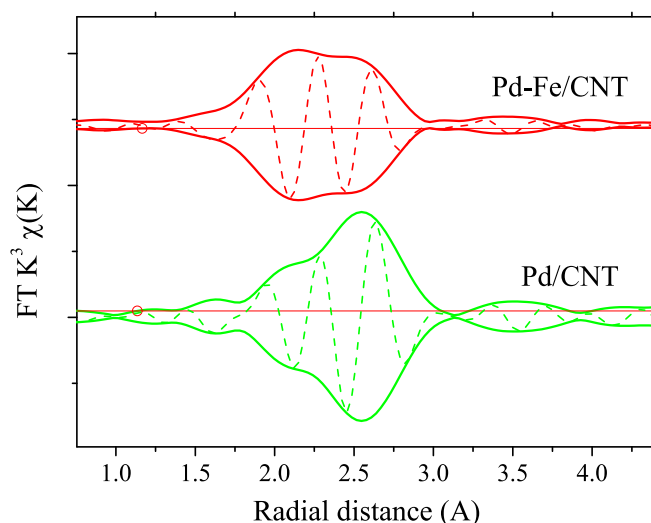


**Fig. 10.** K<sup>3</sup>-weighted modulus and imaginary part of the Fourier transform of Pd K-edge EXAFS spectra at room temperature corresponding to the fresh-reduced cata.

both the monometallic and the bimetallic samples than for foil, which can be explained based on Pd NPs sizes suggesting small and similar NPs for both samples, in good agreement with HAADF-STEM analysis results (see Fig. 7). Both samples present lower Pd K-edge energy position values than the reference (spectra first derivative shown in Fig. 8-inset). This suggests a higher electron density of those Pd centers than in the foil (Pd/CNT ~ Pd-Fe/CNT >> Foil).

To examine the electronic differences in more detail, the evolution of oxidized and reduced species as a function of temperature during TPR in H<sub>2</sub> up to 350 °C are studied shown in Fig. 9. As observed, the presence of Fe shifts Pd reduction to higher temperatures (~40 °C of difference).

EXAFS spectra of the fresh-reduced samples are also acquired to study the local structure around Pd atoms. Fig. 10 shows the Fourier transforms of the Pd k<sup>3</sup>-weighted spectra. Their structural parameters determined through curve fitting are summarized in Table S4. On Pd/CNT, the Pd – Pd atomic first coordination shell of bulk Pd metal appears at a characteristic distance of 2.76 Å. However, for Pd-Fe/CNT, another scattering path at shorter distance than the typical Pd–Pd distance is observed. Therefore it is necessary to introduce another coordination shell, Pd – Fe, at smaller distances ( $R = 2.54$  Å) for a suitable fitting (see Table S4). The presence of this Pd – Fe coordination shell evidences the existence of Pd-Fe interaction in the bimetallic sample, probably existing Pd-Fe alloy. The shorter Pd–Fe distance is due to the smaller size of Fe compared to Pd. Meanwhile, Fe also reduces the Pd–Pd

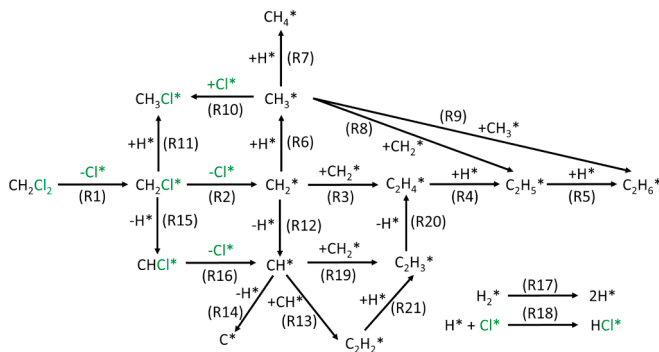


**Fig. 11.** Reaction network of HDC of DCM shows the formation pathways to the main products (C<sub>2</sub>H<sub>4</sub>, CH<sub>4</sub>, C<sub>2</sub>H<sub>6</sub>) and possible subproducts (CH<sub>3</sub>Cl) accompanying the decomposition of H<sub>2</sub> and the formation of HCl (\* refers to active center).



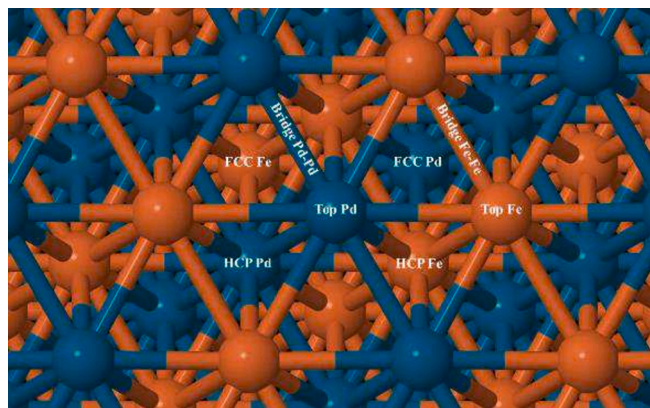


Fig. 12. Position nomenclature on the Pd-Fe(111) (blue ball: Pd atom; orange ball: Fe atom).

neighbour distance ( $R = 2.72 \text{ \AA}$ ).

### 3.3. DFT calculations

Since the incorporation of Fe to Pd catalyst evidently upgrades its stability and the selectivity to light olefins (mainly  $\text{C}_2\text{H}_4$ ), it is very interesting studying the effect of Pd-Fe interaction on the reaction mechanism through DFT calculation studies to understand the reactivity and different selectivity to the products over Pd-Fe centers compared to Pd centers at the atomic level. The HDC of DCM reaction network of all the reaction pathways to produce the main products ( $\text{C}_2\text{H}_4$ ,  $\text{CH}_4$ , and  $\text{C}_2\text{H}_6$ ), possible subproduct  $\text{CH}_3\text{Cl}$  (MCM), and C is shown in Fig. 11. The most stable adsorbed positions of the reactants, intermediate radicals, and products over the Pd-Fe(111) and Pd(111) facets are summarized in Table S5. The position nomenclature on Pd-Fe(111) is shown in Fig. 12. Their associated Gibbs energies for the kinetic and

thermodynamic parameters of the reaction are listed in Tables S6 and S7 respectively (Table S6: Pd-Fe(111); Table S7: Pd(111)). Different pathways for the formation of the  $\text{C}_2\text{H}_4$ ,  $\text{CH}_4$ , and  $\text{C}_2\text{H}_6$  over the same facet are compared, shown in Figs. S6-S11. The Gibbs energy profiles of the most feasible reaction profiles for the main products ( $\text{C}_2\text{H}_4$ ,  $\text{CH}_4$ , and  $\text{C}_2\text{H}_6$ ) over the two mentioned facets are shown in Figs. 13 and 14.

As shown in Fig. 11, the reaction networks begin with the dissociative adsorption of the  $\text{CH}_2\text{Cl}_2$  and  $\text{H}_2$ . The adsorption of  $\text{CH}_2\text{Cl}_2$ , as well as that of  $\text{H}_2$ , are endothermic at the reaction temperature ( $350^\circ\text{C}$ ) over both facets (Pd-Fe(111):  $\text{CH}_2\text{Cl}_2$ : 0.26 eV;  $\text{H}_2$ : 0.46 eV; Pd(111):  $\text{CH}_2\text{Cl}_2$ : 0.20 eV;  $\text{H}_2$ : 0.34 eV, which is contrary with the previous studies working at room temperature [49,50]. This suggests that the high reaction temperature gives some difficulty to the adsorption of the reactants. On one side, the adsorption of  $\text{H}_2$ , as well as its dissociation to  $\text{H}^*$  (0.11 eV), seems more difficult over Pd-Fe(111) than over Pd(111), where it could happen without a barrier of energy (see Tables S6 and S7). Although the preferred adsorption site of  $\text{H}_2$  is on the top of Pd atoms, like its adsorption over Pd(111) (see Table S5), the presence of Fe changes the electronic and geometrical properties of Pd, resulting in the changes of adsorption positions of species (see Table S5) along with their adsorption or desorption energies and activation energies (see Tables S6 and S7). As a result, on Pd-Fe(111), the physisorption of  $\text{H}_2$  on the Pd atoms becomes weaker than that on Pd(111), and the decomposition of  $\text{H}_2$  becomes more difficult on Pd-Fe(111). On the other side, the cleavage of the second C-Cl bond (0.48 eV) seems easier than the first C-Cl (0.58 eV) over Pd(111) and even happens spontaneously without a barrier of energy over Pd-Fe(111) planes. A similar tendency has been noticed in some previous hydrodechlorination works [49–51]. Since the cleavage of  $\text{CH}_2\text{Cl}^*$  occurs over the bridge sites Fe-Fe on Pd-Fe(111) or Pd-Pd on Pd(111), the formed  $\text{CH}_2^*$  locates in the fcc hollow sites (Pd-Fe(111): fcc Pd; Pd(111): fcc) where the valence of C can be fully filled by the incorporation with several metal atoms. Surprisingly, the Fe in the Pd-Fe(111) presents a better dechlorination ability than the Pd in the Pd(111). The excellent dehalogenation ability of Fe atoms has also been

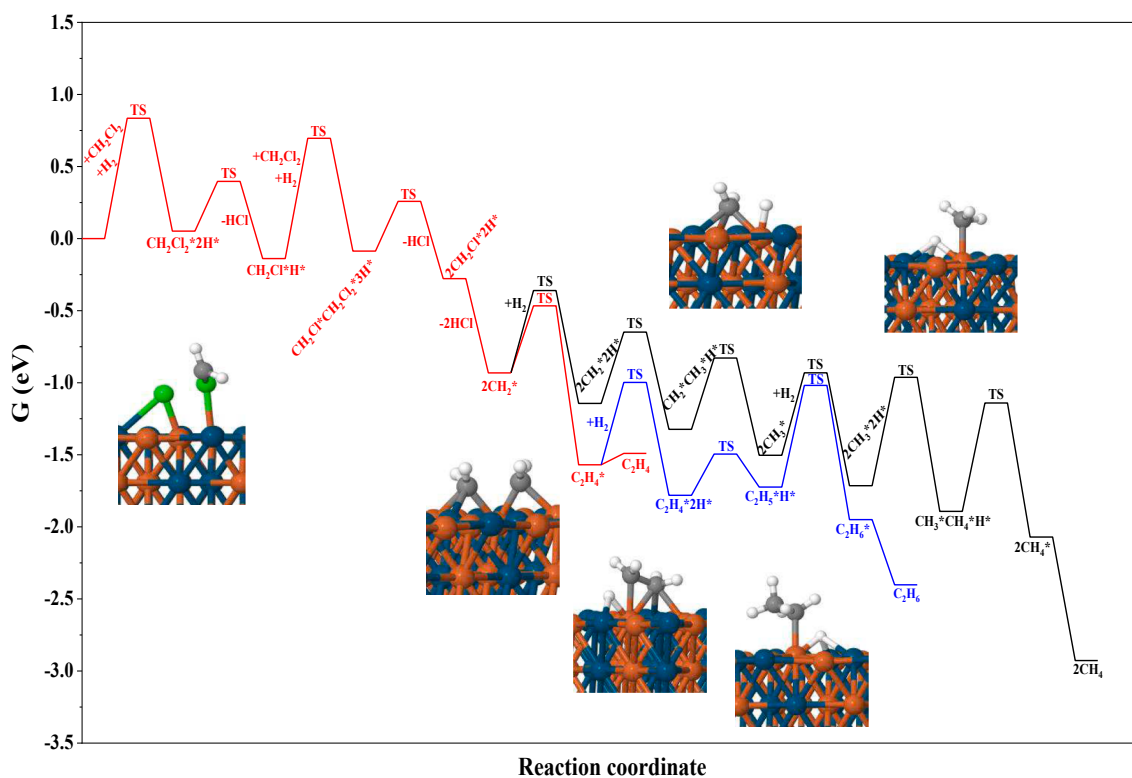
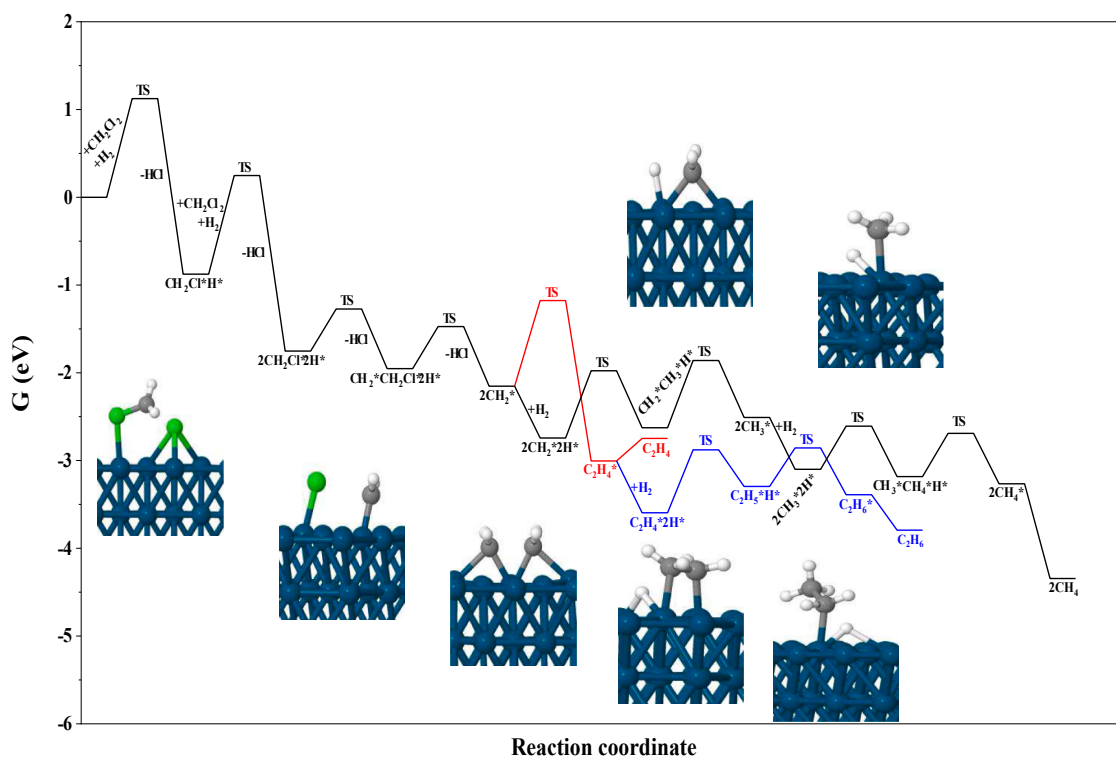


Fig. 13. Energy profiles in HDC of DCM for the formation of  $\text{C}_2\text{H}_4$ ,  $\text{CH}_4$ , and  $\text{C}_2\text{H}_6$  on Pd-Fe(111) (\*: Active Center; Imagens present the main transition states in the reaction pathways; blue ball: Pd atom; orange ball: Fe atom; grey ball: C atom; white ball: H atom; green ball: Cl atom).



**Fig. 14.** Energy profiles in HDC of DCM for the formation of  $C_2H_4$ ,  $CH_4$ , and  $C_2H_6$  on Pd(111) (\*: Active Center; Imagens present the main transition states in the reaction pathways; blue ball: Pd atom; grey ball: C atom; white ball: H atom; green ball: Cl atom).

considered in another hydrodehalogenation study [52]. In this work, the experimental results show that the Pd-Fe/CNT presents much higher stability than Pd/CNT (see Fig. 2(a)) which can be related to the remarkable dechlorination ability of Fe atoms as predicted by the DFT calculations. However, chlorides can be adsorbed on the interacted Pd-Fe surface coinciding with the XPS analysis results. It could be confirmed that high covering of dissociated H atoms from  $H_2$  is necessary for Pd-Fe centers to remove the large amounts of adsorbed Cl atoms through the formation of HCl (see Table S6), which explains the evident deactivation of Pd-Fe/CNT when reducing the  $H_2$ /DCM molar ratio from 50 to 25 in the experimental study (see Fig. 3(a)).

The dehydrogenation of  $CH_2Cl^*$  to produce  $CHCl^*$  is also studied over both facets (see Tables S6 and S7). However, compared to the cleavage of C-Cl, the dehydrogenation meets a higher barrier of energy on the Pd(111) (0.73 eV) and cannot occur over Pd-Fe(111). On the other side, the excess  $H_2$  proportion is set in the experiments ( $H_2$ /DCM = 50–25, see Figs. 2 and 3). Hence, the dehydrogenation is inhibited in this work.

Then, the as-formed  $CH_2^*$  participates in the formation of main products ( $C_2H_4$ ,  $CH_4$ , and  $C_2H_6$ ), possible byproduct ( $CH_3Cl$ ), and C over both facets. Firstly, different routes for forming  $C_2H_4$  are studied (see Figs. S6 and S9). On Pd-Fe(111), the formation of  $C_2H_4$  through the coupling of two  $CH_2^*$  requires a lower activation energy barrier (0.47 eV) than that on Pd(111) (0.98 eV). Besides, a nearly thermoneutral energy (0.08 eV) is required in the desorption of  $C_2H_4$  on Pd-Fe(111), while a higher barrier is required (0.26 eV) on Pd(111). Herein, the formation of  $C_2H_4$  seems more feasible on Pd-Fe(111). Although, on both facets (see Tables S6 and S7), the dehydrogenation of  $CH_2^*$  to form  $CH^*$  (0.31 eV (Pd-Fe(111)); 0.19 eV (Pd(111))) is more favored than the direct formation of  $C_2H_4^*$  through the coupling of two  $CH_2^*$  (0.46 eV (Pd-Fe(111)); 0.98 eV (Pd(111))), the formed  $CH^*$  needs to pass 2 or 3 more elementary steps with relatively high barriers of energy to form the  $C_2H_4^*$  on both facets (see Figs. S6 and S9, Tables S6 and S7). Elsewhere, as mentioned previously, dehydrogenation is not favored in the employed experimental conditions. Therefore, on both facets, coupling

two  $CH_2^*$  to form  $C_2H_4^*$  seems more feasible than the dehydrogenation of  $CH_2^*$ . The reaction profiles of the hydrogenation of  $CH_2^*$  to form  $CH_4$  over both facets are shown in Figs. S7 and S10. As the dehydrogenation of  $CH_2^*$  to  $CH^*$  is not favored, the  $CH_2^*$  will be continually hydrogenated to  $CH_4$  with several elementary steps collaborating with  $H^*$  coming from the  $H_2$  dissociative adsorption. Moreover, the formation of  $C_2H_6$  is also studied through different routes over both facets (see Figs. S8 and S11).  $C_2H_6^*$  could be formed through the two-step hydrogenations of  $C_2H_4^*$  or through the direct coupling reaction of two formed  $CH_3^*$  or coupling of  $CH_3^*$  with  $CH_2^*$  to form an intermediate  $C_2H_5^*$  which will proceed with the hydrogenation to  $C_2H_6^*$ . Among the three pathways, the coupling reaction of two formed  $CH_3^*$  requires great barriers of energy on both facets (Pd-Fe(111): 1.84 eV; Pd(111): 2.22 eV). Although the coupling of  $CH_3^*$  with  $CH_2^*$  to form  $C_2H_5^*$  requires lower activation energy barriers (Pd-Fe(111): 0.78 eV; Pd(111): 1.20 eV), they are still higher than the barriers in the first step hydrogenation of  $C_2H_4^*$  (Pd-Fe(111): 0.29 eV; Pd(111): 0.72 eV). Meanwhile, the hydrogenation of  $C_2H_5^*$  requires lower barriers (Pd-Fe(111): 0.71 eV; Pd(111): 0.44 eV) than those required in the coupling of two  $CH_3^*$  on both facets. Therefore, the formation of  $C_2H_6$  via the hydrogenation of  $C_2H_4^*$  seems more feasible over both facets.

In addition, as the  $CH_3Cl$  has been observed in some previous HDC of DCM studies [53,54], the possibility of its formation over both facets is also discussed (see Tables S6 and S7). The  $CH_3Cl$  could be formed by coupling  $CH_3^*$  with a free neighboring  $Cl^*$  or the coupling of  $CH_2Cl^*$  with a free  $H^*$ . It seems that the  $CH_3^*$  prefers to couple with an  $H^*$  to form  $CH_4^*$  (Pd-Fe(111): 0.75 eV; Pd(111): 0.49 eV) than to couple with a  $Cl^*$  owing to its higher activation energy barrier over both facets (Pd-Fe(111): 2.14 eV; Pd(111): 1.79 eV). Furthermore, the reverse activation energy barriers of the coupling of  $CH_3^*$  with  $Cl^*$  (Pd-Fe(111): 0.69 eV; Pd(111): 1.04 eV) are lower than in the forward reaction over both facets. Therefore, the formation of  $CH_3Cl$  over both facets would be suppressed in this route. On the other side, as mentioned, the  $CH_2Cl^*$  could be decomposed into  $CH_2^*$  and  $Cl^*$  without any barrier over Pd-Fe(111). Thus, the hydrogenation of  $CH_2Cl^*$  to  $CH_3Cl^*$  with an activation

energy barrier of 0.60 eV would not occur over Pd-Fe(111). Meanwhile, on Pd(111), the hydrogenation of  $\text{CH}_2\text{Cl}^*$  also seems complicated to take place due to its higher barrier (0.77 eV) than its dechlorination to  $\text{CH}_2^*$  (0.48 eV). Herein, the theoretical calculations suggest that the formation of  $\text{CH}_3\text{Cl}$  should hardly occur over both facets, coinciding with the observed experimental results (see Fig. 2(b) and S1(a and b)).

Elsewhere, the possible formation of C on both facets is also studied (see Tables S6 and S7). The mean route of carbon formation would be the total dehydrogenation of  $\text{CH}_2^*$ . As has been previously mentioned, the dehydrogenation of  $\text{CH}_2^*$  to  $\text{CH}^*$  requires a low barrier over both facets, while the continual dehydrogenation of  $\text{CH}^*$  to  $\text{C}^*$  is fairly endothermic ( $\Delta E$ : Pd-Fe(111): 0.22 eV; Pd(111): 0.21 eV) and requires much higher activation energy barriers over both facets (Pd-Fe(111): 0.84 eV; Pd(111): 1.10 eV), and their revised barriers are lower (Pd-Fe(111): 0.62 eV; Pd(111): 0.89 eV). Thus, the formation of  $\text{C}^*$  should not happen, especially at experimental conditions with an excess  $\text{H}_2$  proportion, in good correlation with the XPS analysis results where the formation of  $\text{PdC}_x$  is not observed in the used catalysts (see Fig. 5).

The most feasible reaction profiles of main products  $\text{C}_2\text{H}_4$ ,  $\text{CH}_4$ , and  $\text{C}_2\text{H}_6$  over both facets are summarized in Figs. 13 and 14. On the Pd-Fe(111) (see Fig. 13), the total dechlorinated  $\text{CH}_2^*$  prefers to couple with another  $\text{CH}_2^*$  to form  $\text{C}_2\text{H}_4^*$  (0.47 eV) than to be continually hydrogenated to form a  $\text{CH}_3^*$  (0.50 eV). Furthermore, the dissociative adsorption of  $\text{H}_2^*$  over Pd-Fe(111) also improves the activation energy barrier of this hydrogenation process (adsorption energy of  $\text{H}_2$ : 0.458 eV; activation energy barrier: 0.11 eV) to form a  $\text{CH}_3^*$  (0.50 eV). In addition, the desorption of  $\text{C}_2\text{H}_4$  is nearly thermoneutral (0.08 eV), which is much more favorable than its continual hydrogenation to form  $\text{C}_2\text{H}_5$  (0.29 eV). Therefore, the  $\text{C}_2\text{H}_4$  is considered as the kinetically most favorable product on Pd-Fe(111), showing a good agreement with the highest  $\text{C}_2\text{H}_4$  selectivity in the experimental results employing Pd-Fe/CNT (see Fig. S1(b)). Moreover,  $\text{C}_2\text{H}_4^*$  and  $\text{CH}_2^*$  are intermediates that could be continually hydrogenated to form  $\text{C}_2\text{H}_6$  and  $\text{CH}_4$ , respectively. Thus, the experimental results show that when reducing the  $\text{H}_2$  proportion (reducing  $\text{H}_2/\text{DCM}$  molar ratio from 50 to 25), although the catalyst deactivates more quickly, the selectivity to  $\text{C}_2\text{H}_4$  together with its yield increase (see Fig. 3(b), 4 and S2), while the selectivities to the other two products decrease (see Fig. 3(b) and S2). Between the two products ( $\text{CH}_4$  and  $\text{C}_2\text{H}_6$ ), the selectivity to  $\text{CH}_4$  is higher than that to  $\text{C}_2\text{H}_6$  (see Fig. S1(b)), owing to the higher thermodynamical stability of  $\text{CH}_4$  over Pd-Fe(111) (see Fig. 13).

In the case of Pd(111) (see Fig. 14), the total dechlorinated  $\text{CH}_2^*$  prefers to incorporate a  $\text{H}^*$  to form  $\text{CH}_3^*$  (0.766 eV) due to the strong hydrogenation ability of Pd(111) consequence of the spontaneous dissociation of  $\text{H}_2$  to  $\text{H}^*$ , whereas the coupling with another  $\text{CH}_2^*$  requires slightly higher barrier (0.98 eV). Herein, the  $\text{CH}_4$  becomes the kinetically and thermodynamically most favorable product over Pd(111) in agreement with its highest selectivity observed on Pd/CNT (see Fig. 2(b) and S1(a)) with an excess  $\text{H}_2$  environment ( $\text{H}_2/\text{DCM} = 50$ ). On the other hand, the desorption of  $\text{C}_2\text{H}_4$  on Pd(111) is much more endothermic (0.26 eV) than that on Pd-Fe(111). The strong hydrogenation ability of Pd(111) also makes the hydrogenation of  $\text{C}_2\text{H}_4^*$  to  $\text{C}_2\text{H}_6$  more stable and feasible (see Fig. 14). As a result, the  $\text{C}_2\text{H}_4$  becomes the most inhibited product on Pd(111) in agreement with its lowest selectivity among the three products, while the  $\text{C}_2\text{H}_6$  becomes the second more selective product shown by the experimental results (see Fig. 2(b) and S1(a)).

Therefore, a good agreement is achieved between the theoretical models and the experimental results; the existence of Pd-Fe interaction give the Pd-Fe/CNT a more stable activity with a remarkable selectivity to  $\text{C}_2\text{H}_4$  compared to the other 3 catalysts.

#### 4. Conclusions

In this work, Pd-Fe/CNT shows a good performance in the HDC of DCM owing to the existence of a stable Pd-Fe interaction. It shows a high

DCM conversion (initial conversion: ca. 81 %) with the highest stability among the four catalysts tested (Pd/CNT, Pd-Fe/CNT Pd-Sn/CNT, and Pd-Ag/CNT) owing to the incorporation of Fe to Pd catalyst which evidently improves its stability. Furthermore, Pd-Fe/CNT also shows the highest selectivity to olefins (>60 %, mainly  $\text{C}_2\text{H}_4$ , at a conversion of ca. 81 %), operating with  $\text{H}_2/\text{DCM} = 50$  and a temperature of 350 °C. Reducing the  $\text{H}_2/\text{DCM}$  molar ratio from 50 to 25 leads to higher selectivity to olefins but with more rapid deactivation. Pd-Fe/CNT catalyst achieves a significant improvement in terms of activity and selectivity to olefins when compared to the rest of the synthesized catalysts. Elsewhere, compared to Pd-Fe/CNT, the other three tested catalysts deactivate much faster under the same operating conditions,  $\text{CH}_4$  being the main reaction product, especially on Pd-Sn/CNT.

Small NPs as active centers are shown in the fresh-reduced and used catalysts except in the case of Pd-Ag/CNT, where big Ag NPs appear in both. On the other side, high electron density of the Pd centers on both Pd-Fe/CNT and Pd/CNT is confirmed by XANES analysis. Therefore, the good performance shown by Pd-Fe/CNT in the HDC of DCM to olefins can be mainly attributed to the existence of Pd-Fe interaction confirmed by this technique.

The DFT calculations are in good agreement with the experimental results, showing reaction mechanisms that explain the selectivity to the main products at atomic level on pure Pd centers, and the influence of incorporating Fe to them. Incorporating Fe atoms into the Pd lattice changes its electronic and geometrical properties.  $\text{C}_2\text{H}_4$  and  $\text{CH}_4$  are the main reaction products with Pd-Fe/CNT and Pd/CNT, respectively. On the studied Pd-Fe(111), the  $\text{CH}_2\text{Cl}_2$  can be completely dechlorinated with much lower activation energy compared to that on the studied pure Pd(111), which is related to the better dechlorination ability of Fe than Pd. On the other hand, the formation of  $\text{C}_2\text{H}_4$  from  $\text{CH}_2^*$  is favored versus its further hydrogenation to  $\text{CH}_4$  on Pd-Fe(111). However, unlike Pd(111), on Pd-Fe(111),  $\text{H}_2$  splitting cannot occur spontaneously, somewhat activation energy is necessary which give some obstacles to the subsequent hydrogenations of  $\text{C}_2\text{H}_4$  to  $\text{C}_2\text{H}_6$ . Therefore, the formation of  $\text{C}_2\text{H}_4$  on Pd-Fe(111) is favored, although it is still influenced by the  $\text{H}_2$  proportion. When reducing the  $\text{H}_2/\text{DCM}$  molar ratio, Pd-Fe/CNT suffers a stronger deactivation. To maintain the high activity of Pd-Fe/CNT, high covering of  $\text{H}_2$  is needed to remove the adsorbed Cl atoms by the formation of HCl, preventing the adsorption of other chlorides. However, the selectivity and yield of  $\text{C}_2\text{H}_4$  increases when decreasing the  $\text{H}_2/\text{DCM}$  molar ratio.

The DFT calculations also shows high activation energy barriers in the formation of  $\text{C}^*$  on Pd-Fe(111) and Pd(111), which coincides with no formation of  $\text{PdC}_x$  on both used catalysts confirmed by the characterization analysis.

On the other hand, bimetallic NPs with a homogeneous metal distribution, are observed in Pd-Sn/CNT. As a consequence, the difficulty of Sn atoms to adsorb any carbon atom hinders the activity of the catalyst, becoming  $\text{CH}_4$  the main product, with 94 % selectivity at a conversion of ca. 72 % with a low stability which could be mainly ascribed to the instable Pd-Sn interaction. Elsewhere, Pd-Ag/CNT also shows an instable Pd-Ag interaction and a significant amount of monometallic Ag NPs, presenting similar activity and selectivity distribution than Pd/CNT. Furthermore, big Ag NPs and their sintering and oxidation during the reaction negatively affected the activity of Pd-Ag/CNT.

#### CRedit authorship contribution statement

**Sichen Liu:** Writing – review & editing, Writing – original draft, Validation, Methodology, Investigation, Formal analysis, Data curation, Conceptualization. **Ana Iglesias-Juez:** Writing – review & editing, Writing – original draft, Validation, Resources, Methodology, Investigation, Formal analysis, Data curation. **Ana B. Hungria:** Resources, Investigation, Methodology, Formal analysis, Validation, Data curation, Writing – original draft, Writing – review & editing, Supervision. **Maria Martin-Martinez:** Writing – review & editing, Validation, Supervision,



Methodology, Investigation, Funding acquisition, Data curation, Conceptualization. **Jorge Bedia**: Writing – review & editing, Validation, Supervision, Methodology, Investigation, Conceptualization. **Juan José Rodríguez**: Writing – review & editing, Supervision. **Luisa María Gómez-Sainero**: Writing – review & editing, Validation, Supervision, Project administration, Methodology, Investigation, Funding acquisition, Formal analysis, Data curation, Conceptualization.

### Declaration of competing interest

The authors declare the following financial interests/personal relationships which may be considered as potential competing interests: Luisa María Gómez-Sainero reports financial support was provided by Ministerio de Ciencia Innovación y Universidades Agencia Estatal de investigación CTM2017-85498-R. Luisa Maria Gomez Sainero reports financial support was provided by ALBA Synchrotron facility for beamtime at CLAESS (experiment 2016021666-2). Maria Martin Martinez reports financial support was provided by Comunidad de Madrid-UAM SI1/PJI/2019-00487. Ana B. Hungria reports financial support was provided by Junta de Andalucía (P20\_00968). Maria Martin Martinez reports financial support was provided by Comunidad de Madrid Programa atraccion de talento 2017\_T2/AMB.5668. Sichen Liu reports financial support was provided by Research grant (PRE2018-084424), Ministerio de Ciencia e Innovación. Sichen Liu reports his research stay realized in Group of Professor Núria López at Institut Català d'Investigació Química (Tarragona, Spain). If there are other authors, they declare that they have no known competing financial interests or personal relationships that could have appeared to influence the work reported in this paper.

### Data availability

Data will be made available on request.

### Acknowledgments

The authors acknowledge FEDER/Ministerio de Ciencia, Innovación y Universidades – Agencia Estatal de Investigación (CTM2017-85498-R), Comunidad de Madrid/UAM (SI1/PJI/2019-00487) and Junta de Andalucía (P20\_00968) for financial support. The authors acknowledge the ALBA Synchrotron facility and Dr. Carlo Marini for beamtime at CLAESS (experiment 2016021666-2) and the contribution of the group of Professor Núria López at Institut Català d'Investigació Química (Tarragona, Spain). Maria Martin-Martinez acknowledges a post-doctoral grant (2017-T2/AMB.5668) from the Comunidad de Madrid “Atracción de Talento” program. Sichen Liu acknowledges Ministerio de Ciencia e Innovación for his research grant (PRE2018-084424).

### Appendix A. Supplementary data

Supplementary data to this article can be found online at <https://doi.org/10.1016/j.cej.2024.152128>.

### References

- [1] B. Huang, C. Lei, C. Wei, G. Zeng, Chlorinated volatile organic compounds (Cl-VOCs) in environment — sources, potential human health impacts, and current remediation technologies, *Environ. Int.* 71 (2014) 118–138, <https://doi.org/10.1016/j.envint.2014.06.013>.
- [2] M. Martin-Martinez, L.M. Gómez-Sainero, M.A. Alvarez-Montero, J. Bedia, J. J. Rodríguez, Comparison of different precious metals in activated carbon-supported catalysts for the gas-phase hydrodechlorination of chloromethanes, *Appl. Catal. B Environ.* 132–133 (2013) 256–265, <https://doi.org/10.1016/j.apcatb.2012.11.041>.
- [3] M. Martin-Martinez, L.M. Gómez-Sainero, J. Bedia, A. Arevalo-Bastante, J. J. Rodríguez, Enhanced activity of carbon-supported Pd–Pt catalysts in the hydrodechlorination of dichloromethane, *Appl. Catal. B Environ.* 184 (2016) 55–63, <https://doi.org/10.1016/j.apcatb.2015.11.016>.
- [4] C. Fernandez-Ruiz, J. Bedia, S. Andreoli, S. Eser, J.J. Rodríguez, L.M. Gómez-Sainero, Selectivity to olefins in the hydrodechlorination of chloroform with activated carbon-supported palladium catalysts, *Ind. Eng. Chem. Res.* 58 (2019) 20592–20600, <https://doi.org/10.1021/acs.iecr.9b04262>.
- [5] M. Gamero, A.T. Aguayo, A. Ateka, P. Pérez-Urriarte, A.G. Gayubo, J. Bilbao, Role of shape selectivity and catalyst acidity in the transformation of chloromethane into light olefins, *Ind. Eng. Chem. Res.* 54 (2015) 7822–7832, <https://doi.org/10.1021/acs.iecr.5b01745>.
- [6] L.-T. Kong, B.-X. Shen, J.-G. Zhao, J.-C. Liu, Comparative study on the chloromethane to olefins reaction over SAPO-34 and HZSM-22, *Ind. Eng. Chem. Res.* 53 (2014) 16324–16331, <https://doi.org/10.1021/ie5028155>.
- [7] L.-T. Kong, B.-X. Shen, Z. Jiang, J.-G. Zhao, J.-C. Liu, Synthesis of SAPO-34 with the presence of additives and their catalytic performance in the transformation of chloromethane to olefins, *React. Kinet. Mech. Catal.* 114 (2015) 697–710, <https://doi.org/10.1007/s11444-014-0812-1>.
- [8] Y. Wei, D. Zhang, Z. Liu, B.-L. Su, Methyl halide to olefins and gasoline over zeolites and SAPO catalysts: A new route of MTO and MTG, *Chin. J. Catal.* 33 (2012) 11–21, [https://doi.org/10.1016/S1872-2067\(10\)60303-8](https://doi.org/10.1016/S1872-2067(10)60303-8).
- [9] L.M. Gómez-Sainero, J. Palomar, S. Omar, C. Fernández, J. Bedia, A. Álvarez-Montero, J.J. Rodríguez, Valorization of chloromethanes by hydrodechlorination with metallic catalysts, *Catal. Today* 310 (2018) 75–85, <https://doi.org/10.1016/j.cattod.2017.05.006>.
- [10] C. Fernandez-Ruiz, S. Liu, J. Bedia, J.J. Rodríguez, L.M. Gómez-Sainero, Enhanced selectivity to olefins in the hydrodechlorination of trichloromethane using Ag-Pd on activated carbon catalysts, *J. Environ. Chem. Eng.* 9 (2021) 104744, <https://doi.org/10.1016/j.jece.2020.104744>.
- [11] S. Liu, C. Fernandez-Ruiz, A. Iglesias-Juez, M. Martin-Martinez, J. Bedia, C. Marini, G. Agostini, J.J. Rodríguez, L.M. Gómez-Sainero, Structure sensitivity reaction of chloroform hydrodechlorination to light olefins using Pd catalysts supported on carbon nanotubes and carbon nanofibers, *J. Colloid Interface Sci.* 648 (2023) 427–439, <https://doi.org/10.1016/j.jcis.2023.05.169>.
- [12] C. Fernandez-Ruiz, J. Bedia, J.M. Grau, A.C. Romero, D. Rodríguez, J.J. Rodríguez, L.M. Gómez-Sainero, Promoting light hydrocarbons yield by catalytic hydrodechlorination of residual chloromethanes using palladium supported on zeolite catalysts, *Catalysts* 10 (2020) 199, <https://doi.org/10.3390/catal10020199>.
- [13] E.V. Golubina, E.S. Lokteva, T.S. Lazareva, B.G. Kostyuk, V.V. Lunin, V.I. Simagina, I.V. Stoyanova, Hydrodechlorination of tetrachloromethane in the vapor phase in the presence of Pd–Fe/Sibunit catalysts, *Kinet. Catal.* 45 (2) (2004) 183–188, <https://doi.org/10.1023/B:KICA.0000023789.28190.1b>.
- [14] R. Tao, Z. Sun, Y. Xie, H. Zhang, C. Huang, Y. Zhao, Z. Liu, In situ loading of palladium nanoparticles on mica and their catalytic applications, *J. Colloid. Interface. Sci.* 353 (2011) 269–274, <https://doi.org/10.1016/j.jcis.2010.09.027>.
- [15] M. Martin-Martinez, A. Álvarez-Montero, L.M. Gómez-Sainero, R.T. Baker, J. Palomar, S. Omar, S. Eser, J.J. Rodríguez, Deactivation behavior of Pd/C and Pt/C catalysts in the gas-phase hydrodechlorination of chloromethanes: Structure–reactivity relationship, *Appl. Catal. B Environ.* 162 (2015) 532–543, <https://doi.org/10.1016/j.apcatb.2014.07.017>.
- [16] P. Serp, E. Castillejos, Catalysis in carbon nanotubes, *ChemCatChem* 2 (2010) 41–47, <https://doi.org/10.1002/cctc.200900283>.
- [17] Y. Yan, J. Miao, Z. Yang, F.-X. Xiao, H.B. Yang, B. Liu, Y. Yang, Carbon nanotube catalysts: recent advances in synthesis, characterization and applications, *Chem. Soc. Rev.* 44 (2015) 3295–3346, <https://doi.org/10.1039/c4cs00492b>.
- [18] P. Serp, M. Corrias, P. Kalck, Carbon nanotubes and nanofibers in catalysis, *Appl. Catal. A: Gen.* 253 (2003) 337–358, [https://doi.org/10.1016/S0962-860X\(03\)00549-0](https://doi.org/10.1016/S0962-860X(03)00549-0).
- [19] Z. Sun, Y. Zhao, Y. Xie, R. Tao, H. Zhang, C. Huang, Z. Liu, The solvent-free selective hydrogenation of nitrobenzene to aniline: an unexpected catalytic activity of ultrafine Pt nanoparticles deposited on carbon nanotubes, *Green Chem.* 12 (2010) 1007–1011, <https://doi.org/10.1039/c002391d>.
- [20] C.D. Wagner, L.E. Davis, M.V. Zeller, J.A. Taylor, R.H. Raymond, L.H. Gale, Empirical atomic sensitivity factors for quantitative analysis by electron spectroscopy for chemical analysis, *Surf. Interface Anal.* 3 (1981) 211–225, <https://doi.org/10.1002/sia.740030506>.
- [21] B. Ravel, M. Newville, ATHENA, ARTEMIS, HEPHAESTUS: data analysis for X-ray absorption spectroscopy using IFEFFIT, *J. Synchrotron Rad.* 12 (2005) 537–541, <https://doi.org/10.1107/S0909049505012719>.
- [22] Z.M. de Pedro, L.M. Gómez-Sainero, E. Gonzalez-Serrano, J.J. Rodríguez, Gas-Phase hydrodechlorination of dichloromethane at low concentrations with palladium/carbon catalysts, *Ind. Eng. Chem. Res.* 45 (2006) 7760–7766, <https://doi.org/10.1021/ie060621m>.
- [23] G. Kresse, J. Furthmüller, Efficiency of ab-initio total energy calculations for metals and semiconductors using a plane-wave basis set, *Comput. Mater. Sci.* 6 (1996) 15–50, [https://doi.org/10.1016/0927-0256\(96\)00008-0](https://doi.org/10.1016/0927-0256(96)00008-0).
- [24] G. Kresse, J. Furthmüller, Efficient iterative schemes for ab initio total-energy calculations using a plane-wave basis set, *Phys. Rev. B* 54 (1996) 11169–11186, <https://doi.org/10.1103/physrevb.54.11169>.
- [25] J.P. Perdew, K. Burke, M. Ernzerhof, Generalized gradient approximation made simple, *Phys. Rev. Lett.* 77 (1996) 3865–3868, <https://doi.org/10.1103/PhysRevLett.77.3865>.
- [26] S. Grimme, J. Antony, S. Ehrlich, H. Krieg, A consistent and accurate ab initio parametrization of density functional dispersion correction (DFT-D) for the 94 elements H–Pu, *J. Chem. Phys.* 132 (2010) 154104, <https://doi.org/10.1063/1.3382344>.



- [27] R.V. Chepulsii, S.V. Barabash, A. Zunger, Ab initio theory of phase stability and structural selectivity in Fe-Pd alloys, *Phys. Rev. B* 85 (2012) 144201, <https://doi.org/10.1103/PhysRevB.85.144201>.
- [28] G. Henkelman, H. Jónsson, Improved tangent estimate in the nudged elastic band method for finding minimum energy paths and saddle points, *J. Chem. Phys.* 113 (2000) 9978–9985, <https://doi.org/10.1063/1.1323224>.
- [29] G. Henkelman, B.P. Uberuaga, H. Jónsson, A climbing image nudged elastic band method for finding saddle points and minimum energy paths, *J. Chem. Phys.* 113 (2000) 9901–9904, <https://doi.org/10.1063/1.1329672>.
- [30] V. Wang, N. Xu, J.-C. Liu, G. Tang, W.-T. Geng, VASPKIT: a user-friendly interface facilitating high-throughput computing and analysis using VASP code, *Comput. Phys. Commun.* 267 (2021) 108033, <https://doi.org/10.1016/j.cpc.2021.108033>.
- [31] J.F. Moulder, W.F. Stickle, P.E. Sobol, K.D. Bomben, *Handbook of X-Ray Photoelectron Spectroscopy. A Reference Book of Standard Spectra for Identification and Interpretation of XPS Data*, Perkin-Elmer Corporation Physical Electronics Division, Minnesota, 1992.
- [32] M.A. Álvarez-Montero, L.M. Gómez-Sainero, A. Mayoral, I. Diaz, R.T. Baker, J. J. Rodriguez, Hydrodechlorination of chloromethanes with a highly stable Pt on activated carbon catalyst, *J. Catal.* 279 (2011) 389–396, <https://doi.org/10.1016/j.jcat.2011.02.009>.
- [33] L.M. Gómez-Sainero, J.M. Grau, A. Arcoya, X.L. Seoane, Carbon-supported palladium catalysts for liquid-phase hydrodechlorination of carbon tetrachloride to chloroform, *Stud. Surf. Sci. Catal.* 130 (2000) 2009–2014, [https://doi.org/10.1016/S0167-2991\(00\)80763-6](https://doi.org/10.1016/S0167-2991(00)80763-6).
- [34] D. Wang, J. Liu, J. Xi, J. Jiang, Z. Bai, Pd-Fe dual-metal nanoparticles confined in the interface of carbon nanotubes/N-doped carbon for excellent catalytic performance, *Appl. Surf. Sci.* 489 (2019) 477–484, <https://doi.org/10.1016/j.apsusc.2019.06.039>.
- [35] F. Wang, H. Xue, Z. Tian, W. Xing, L. Feng, Fe<sub>2</sub>P as a novel efficient catalyst promoter in Pd/C system for formic acid electro-oxidation in fuel cells reaction, *J. Power Sources* 375 (2018) 37–42, <https://doi.org/10.1016/j.jpowsour.2017.11.055>.
- [36] M.P. Felicissimo, O.N. Martyanov, T. Risse, H.-J. Freund, Characterization of a Pd–Fe bimetallic model catalyst, *Surf. Sci.* 601 (2007) 2105–2116, <https://doi.org/10.1016/j.susc.2007.02.023>.
- [37] N. Pino, S. Sathisa, Q. Tan, T. Souza, D. López, D.E. Resasco, Structure, activity, and selectivity of bimetallic Pd-Fe/SiO<sub>2</sub> and Pd-Fe/ $\gamma$ -Al<sub>2</sub>O<sub>3</sub> catalysts for the conversion of furfural, *J. Catal.* 350 (2017) 30–40, <https://doi.org/10.1016/j.jcat.2017.03.016>.
- [38] R. Li, Y. Yue, Z. Chen, X. Chen, S. Wang, Z. Jiang, B. Wang, Q. Xu, D. Han, J. Zhao, Selective hydrogenation of acetylene over Pd-Sn catalyst: Identification of Pd<sub>2</sub>Sn intermetallic alloy and crystal plane-dependent performance, *Appl. Catal. b: Environ.* 279 (2020) 119348, <https://doi.org/10.1016/j.apcatb.2020.119348>.
- [39] L. Yan, Y. Wang, L. Zhu, J. Chen, Y. Xu, Z. Wang, T. Song, B. Zhao, X. Chen, R. Li, Sn regulates the electronic structure and metal particles of Pd to improve the hydrogenation performance of 4-nitrophenol, *New J. Chem.* 47 (2023) 3341–3346, <https://doi.org/10.1039/d2nj05292j>.
- [40] R. Li, J. Zhao, D. Han, X. Li, Pd/C modified with Sn catalyst for liquid-phase selective hydrogenation of maleic anhydride to gamma-butyrolactone, *Chin. Chem. Lett.* 28 (2017) 1330–1335, <https://doi.org/10.1016/j.ccl.2017.04.028>.
- [41] A.K. Wahab, M.A. Nadeem, H. Idriss, Hydrogen production during ethylene glycol photoreactions over Ag-Pd/TiO<sub>2</sub> at different partial pressures of oxygen, *Front. Chem.* 7 (2019) 780, <https://doi.org/10.3389/fchem.2019.00780>.
- [42] J. Tang, S. Yamamoto, T. Koitaya, Y. Yoshikura, K. Mukai, S. Yoshimoto, I. Matsuda, J. Yoshinobu, Hydrogen adsorption and absorption on a Pd-Ag alloy surface studied using in-situ X-ray photoelectron spectroscopy under ultrahigh vacuum and ambient pressure, *Appl. Surf. Sci.* 463 (2019) 1161–1167, <https://doi.org/10.1016/j.apsusc.2018.07.078>.
- [43] Z.Q. Li, C.J. Lu, Z.P. Xia, Y. Zhou, Z. Luo, X-ray diffraction patterns of graphite and turbostratic carbon, *Carbon* 45 (2007) 1686–1695, <https://doi.org/10.1016/j.carbon.2007.03.038>.
- [44] W. Chen, X. Pan, M.-G. Willinger, D.S. Su, X. Bao, Facile Autoreduction of Iron Oxide/Carbon Nanotube Encapsulates, *J. Am. Chem. Soc.* 128 (128) (2006) 3136–3137, <https://doi.org/10.1021/ja056721>.
- [45] Y. Meng, A sustainable approach to fabricating Ag nanoparticles/PVA hybrid nanofiber and its catalytic activity, *Nanomaterials* 5 (2015) 1124–1135, <https://doi.org/10.3390/nano5021124>.
- [46] W. Du, K.E. Mackenzie, D.F. Milano, N.A. Deskins, D. Su, X. Teng, Palladium–tin alloyed catalysts for the ethanol oxidation reaction in an alkaline medium, *ACS Catal.* 2 (2012) 287–297, <https://doi.org/10.1021/cs2005955>.
- [47] M.-L. Yang, Y.-A. Zhu, X.-G. Zhou, Z.-J. Sui, D. Chen, First-principles calculations of propane dehydrogenation over PtSn catalysts, *ACS Catal.* 2 (2012) 1247–1258, <https://doi.org/10.1021/cs300031d>.
- [48] A. Iglesias-Juez, A. Kubacka, M. Fernandez-García, M.D. Michiel, M.A. Newton, Nanoparticulate Pd supported catalysts: Size-dependent formation of Pd(I)/Pd(0) and their role in CO elimination, *J. Am. Chem. Soc.* 133 (2011) 4484–4489, <https://doi.org/10.1021/ja110320y>.
- [49] L. Xu, S. Bhandari, J. Chen, J. Glasgow, M. Mavrikakis, Chloroform hydrodechlorination on palladium surfaces: A comparative DFT study on Pd(111), Pd(100), and Pd(211), *Top. Catal.* 63 (2020) 762–776, <https://doi.org/10.1007/s11244-019-01218-6>.
- [50] L. Xu, X. Yao, A. Khan, M. Mavrikakis, Chloroform hydrodechlorination over palladium–gold catalysts: A first-principles DFT study, *ChemCatChem* 8 (2016) 1739–1746, <https://doi.org/10.1002/cctc.201600144>.
- [51] N. Chen, R.M. Rioux, L.A.M.M. Barbosa, F.H. Ribeiro, Kinetic and theoretical study of the hydrodechlorination of CH<sub>4</sub>-xCl<sub>x</sub> (x = 1–4) compounds on palladium, *Langmuir* 26 (2010) 16615–16624, <https://doi.org/10.1021/la1020753>.
- [52] A.J. Saadun, S. Pablo-García, V. Paunović, Q. Li, A. Sabadell-Rendón, K. Kleemann, F. Krumeich, N. López, J. Pérez-Ramírez, Performance of metal-catalyzed hydrodebromination of dibromomethane analyzed by descriptors derived from statistical learning, *ACS Catal.* 10 (2020) 6129–6143, <https://doi.org/10.1021/acscatal.0c00679>.
- [53] M.A. Álvarez-Montero, L.M. Gómez-Sainero, J. Juan-Juan, A. Linares-Solano, J. J. Rodriguez, Gas-phase hydrodechlorination of dichloromethane with activated carbon-supported metallic catalysts, *Chem. Eng. J.* 162 (2010) 599–608, <https://doi.org/10.1016/j.cej.2010.06.002>.
- [54] A.J. Saadun, G. Zichittella, V. Paunović, B.A. Markaide-Aiastui, S. Mitchell, J. Pérez-Ramírez, Epitaxially directed iridium nanostructures on titanium dioxide for the selective hydrodechlorination of dichloromethane, *ACS Catal.* 10 (2020) 528–542, <https://doi.org/10.1021/acscatal.9b04467>.